

Electronic Theses and Dissertations, 2004-2019

2014

Frequency Selective Detection of Infrared Radiation in Uncooled Optical Nano-Antenna Array

Sushrut Modak
University of Central Florida

 Part of the [Electromagnetics and Photonics Commons](#), and the [Optics Commons](#)
Find similar works at: <https://stars.library.ucf.edu/etd>
University of Central Florida Libraries <http://library.ucf.edu>

This Masters Thesis (Open Access) is brought to you for free and open access by STARS. It has been accepted for inclusion in Electronic Theses and Dissertations, 2004-2019 by an authorized administrator of STARS. For more information, please contact STARS@ucf.edu.

STARS Citation

Modak, Sushrut, "Frequency Selective Detection of Infrared Radiation in Uncooled Optical Nano-Antenna Array" (2014). *Electronic Theses and Dissertations, 2004-2019*. 1236.
<https://stars.library.ucf.edu/etd/1236>

FREQUENCY SELECTIVE DETECTION OF INFRARED RADIATION IN UNCOOLED OPTICAL
NANO-ANTENNA ARRAY

by

SUSHRUT MODAK

B.E. Electronics and Telecommunication Engineering, University Of Pune

A thesis submitted in partial fulfillment of the requirements
for the degree of Master of Science in Optics
in the College of Optics and Photonics
at the University of Central Florida
Orlando, Florida

Fall Term
2014

© 2014 Sushrut Modak

ABSTRACT

Mid-infrared (mid-IR) detection and imaging over atmospheric transparent 3-5 μm and 8-12 μm bands are increasingly becoming important for various space, defense and civilian applications. Various kinds of microbolometers offer uncooled detection of IR radiation. However, broadband absorption of microbolometers makes them less sensitive to spectrally resolved detection of infrared radiation and the fabrication is also very tedious involving multiple complex lithography steps. In this study, we designed an optical nano-antenna array based detector with narrow frequency band of operation. The structure consists of a two-element antenna array comprised of a perforated metallic hole array coupled with an underneath disk array which trap incident radiation as dipole currents. The energy is dissipated as electron plasma loss on the hole-disk system inducing close to $\sim 100\%$ absorption of the incident radiation. This near perfect absorption originates from simultaneous zero crossing of real component of permittivity and permeability due to the geometrical arrangement of the two antenna elements which nullifies overall charge and current distributions, prohibiting existence of any propagating electromagnetic modes at resonance. Moreover, the continuous perforated film allows probing of the induced “micro-current” plasma loss on each nano hole-disk pair via a weak bias current. Such optical antenna design enables flexible scaling of detector response over the entire mid-infrared regime by change in the antenna dimensions. Furthermore, the development of simple nanoimprint lithography based large area optical antenna array

fabrication technique facilitates formation of low cost frequency selective infrared detectors.

ACKNOWLEDGMENTS

I would like to thank my advisor Dr. Debashis Chanda for his guidance, patience and support, both in academia and personal life, without which completing this thesis would not have been possible. I would also like to thank Dr. Schoenfeld and Dr. Fathpour for agreeing to be on my thesis committee. I would like to acknowledge Alireza Safaei and Jonathan Lee for their help in data analysis and fabrication processes. A special thanks to Abraham Vazquez-Guardado and Daniel Franklin for their friendship and technical guidance on various projects. I am also thankful to Rachel Franzetta for her assistance with the administrative work and providing me with valuable advice in times of need. I am grateful to the Nanoscience Technology Center for providing me with financial support during my graduate studies. Last but not least, I want to thank my parents for their unending love and support the entire time.

TALBE OF CONTENTS

LIST OF FIGURES.....	viii
1. INTRODUCTION.....	1
1.1 Motivation and objective.....	1
1.2 Infrared optical antenna.....	2
1.3 Proposed two-element optical antenna array IR detector.....	4
2. FREQUENCY SELECTIVE OPTICAL ANTENNA ARRAY ABSORBERS.....	6
2.1 Analysis of Transmission Through Hole-Disk Antenna Array.....	6
2.2 Hole-Disk Antenna Array –Fabrication Process, Results and Discussion	14
2.3 Cavity Coupled Hole-Disk Antenna Array.....	17
2.4 Cavity Coupled Hole-Disk Antenna Array –Results and Discussion -	27
2.5 Numerical Methods	29
2.5.1 Modified Coupled Dipole Approximation (CDA) Method –.....	29
2.5.2 Effective Index Estimation.....	33
2.5.3 Cavity Phase Evaluation.....	36
2.5.4 LSPR vs. Diameter–.....	36
3. MULTISPECTRAL UNCOOLED INFRARED DETECTORS	38
3.1 Detector Pattern design, Master Pattern Writing and Fabrication.....	41
3.2 Measuring Detector Performance Parameters	48
4. CONCLUSION AND FUTURE SCOPE OF WORK.....	56

4.1 Improvements in multispectral uncooled infrared radiation detector.....	56
4.2 Optical Antenna as Broadband Infrared Absorber.....	58
REFERENCES	61

LIST OF FIGURES

Figure 1- (a) A monopole antenna with ground plane functions as a dipole antenna and (b) a monopole antenna on the tip of a NSOM[2]	3
Figure 2- Structure cross section showing fabrication parameters.....	7
Figure 3- (a) Structure layout of hole array coupled with complementary disc array, (b) Transmission calculated from electromagnetic simulation of just the hole (blue), coupled hole-disc array (red) compared to that of theoretical CDA model(black) and (c) electric field distribution in the coupled hole-disc array structure	9
Figure 4- (a) Transmission of the hole-disc array for different RD.(b) different diameters (with constant period.) and (c) different periods (with constant diameter.)	12
Figure 5- Step by step fabrication process of the hole-disc array	15
Figure 6- a) Simulated and measured transmission spectrum for Period $1.14 \mu m$ and Diameter $0.76 \mu m$.The slight mismatch in amplitude is due to the RD of experimental sample being smaller than targeted 280nm, which was used for simulation and (b) Experimental transmission spectra as a function of increasing period.	16
Figure 7- Schematic diagram of the structure under study.....	17
Figure 8- (a) Cavity coupled hole-disc array 3D schematic, (b) Comparison of simulation and CDA spectra for this structure, (c) Electric field profile at the resonance wavelength, (d) Tunability of absorption peak as diameter is scaled keeping D/P ratio = 0.66 and (e) Comparison of simulation and CDA method in locating peak positions of hole-disc array with and without cavity coupling	19

Figure 9- Transmission of the hole-disk array for different diameter ($D/P=0.66$ is kept constant).....	20
Figure 10- (a) (left) Phase shift in cavity mode due to LSPR, (middle) Cavity mode vs. the actual structure absorption as a function of cavity thickness, (right) Transmission from the hole-disk array, (b) Change in cavity resonance position ($\Delta\lambda$) as a function of cavity thickness and (c) Extracted effective refractive index at $C=870\text{nm}$	23
Figure 11- (a) Current density and (b) Power loss density in the structure at the resonance wavelength of $4.41\ \mu\text{m}$	24
Figure 12- Loss processes in the cavity-coupled hole-disk system.....	26
Figure 13- (a) SEM image showing the hole-disk pattern with 5 different periods, (b) corresponding simulated (black) and measured (red) absorption spectra and (c) peak location as a function of diameter for these structures	28
Figure 14- Hole- disc structure schematic diagram	32
Figure 15- Cavity coupled hole-disk structure schematic diagram.....	32
Figure 16- Separation of the structure for calculation of effective index calculation (i)	34
Figure 17- Separation of the structure for calculation of effective index calculation (ii).....	35
Figure 18- A schematic diagram of a basic bolometer	38
Figure 19- Simulations predicting temperature change and heat loss in the structure	40
Figure 20- (a) A schematic diagram of the detector pattern and (b) biasing circuit of the detector	42

Figure 21- 3D Laser writing process (a) with negative photoresist and (b) with positive photoresist.....	44
Figure 22- Step by step description of the nanoimprint lithography process	45
Figure 23- SEM images of the master pattern written with negative resist (a) top view, (b) cross section showing the tapered pattern and the tapered portion around the edges of a pixel and (c) master pattern written with positive resist.....	46
Figure 24 SEM images showing the detector sample (a) during photolithography step and (b) after metallization and lift off.	47
Figure 25- A SEM image of fabricated detector pattern.	48
Figure 26- A schematic diagram of the setup used for characterization of the bolometer...	50
Figure 27- An optical image of the fabricated detector sample. Electrical connections are made to the sample with a low resistance silver adhesive.....	51
Figure 28- Various spectra used in the calculation of incident power on the sample.	52
Figure 29- Parameters measured as a function of bias voltage- (a) noise power spectral density, (b) the corresponding responsivity and the (c) D^*	55
Figure 31- Predicted change in the detector temperature if the substrate is removed completely (b) compared to with substrate case(a).	57
Figure 32- (a) Schematic diagram of a 3 layer hole-disk array structure, (b) and (c) SEM cross-section of fabricated structure ($P = 1740\text{nm}$, $D = 1060\text{nm}$, $RD = 300\text{nm}$ and cavity thickness $C=750\text{nm}$).	59
Figure 33- Simulated and measured spectra from the multilayer hole-disk structure.....	59

Figure 34- Simulated spectra for absorption for different number of layers in multilayer cavity coupled hole-disk antenna array 60

1. INTRODUCTION

1.1 Motivation and objective

The detection and imaging over atmospheric transparent 3-5 μm and 8-12 μm windows in mid-infrared regime are increasingly becoming important for space explorations, spectroscopy, meteorology, chemical/biological identification, short range communication, flame detection, radiation thermometer, target tracking, night vision, remote sensing, leak detection, house damage inspection etc. However, there are two major limitations in mid-IR detection and imaging. First of all due to low photon energy of mid-IR radiation cryogenic cooling is required for high sensitive detection based on low band-gap materials like mercury-cadmium-telluride (HgCdTe). Various kinds of microbolometers primarily based on vanadium oxide (VO_x) offer uncooled detection of IR radiations. However, microbolometers suffer from low sensitivity, slow response and tedious multi-step complex lithographic processes[1]. Second one is absence of spectroscopic or color detection/imaging abilities in the infrared domain. At present all cooled and uncooled mid-IR detectors being “bucket” detectors generate integrated spectral images in binary color format (choices of any two pseudo colors). Also the narrowband infrared absorption spectroscopy has proven to be a very important tool in the detection and identification of airborne chemicals where pattern recognition is used as a post-processing step to compare the infrared spectrum of molecules from a library against the infrared spectra of airborne contaminants. Present broadband detectors are not sensitive enough to perform low concentration chemical detection from IR radiation. In particular, detection sensitivity of

microbolometer arrays operating in the mid-IR region is limited by the blackbody radiation limit. To date very little research work has been performed on frequency selective uncooled devices.

1.2 Infrared optical antenna

The open scientific question is can we detect infrared radiation in the same way radio frequency (RF) is detected by RF antennas over a narrow band across the carrier frequency? An antenna can be described in a simple way as a device, which converts electromagnetic radiation to a measurable electrical signal and its opposite case, a device that converts an electrical signal to electromagnetic radiation. Since its discovery as a novel concept in the beginning of 19th century, it has changed the way we communicate completely. It serves as a fundamental building block of today's complex telecommunication industry. If we look at the optical analog, today's optical technology relies on lenses, mirrors, prisms etc. to control and modify the path of optical beams. This form of control relies on the ray approach or the paraxial approximation of light and sub-wavelength control is not possible. At microwave frequencies, metals are very good conductors of electricity and the antenna used are much larger than the skin depth at that frequency. So, if we simply scale down the size of antenna, it should work in the optical regime as well since Maxwell's equations are scale invariant. But this is not the case as metals are highly dispersive in this region. At optical frequencies, the metal's free electron gas can sustain surface charge density oscillations, called plasmons, which mediate the interaction between metals and electromagnetic radiation. The interaction is enhanced on

the nanostructured metallic surface due to the increase in electron density as propagating surface plasmon polaritons (SPP) and localized surface plasmon (LSP). SPP and LSP are responsible for introduction of additional loss while propagating on metal surface. Because of this reason, most of the success of antenna remains confined to radio and microwave domain and its optical analog is not very developed[2]. Recent developments in plasmonics along with the development in fabrication tools, optical antennas have attracted much attention in the recent years. As results of the presence of surface plasmons, there is a large localization of electromagnetic fields near the antenna surface.

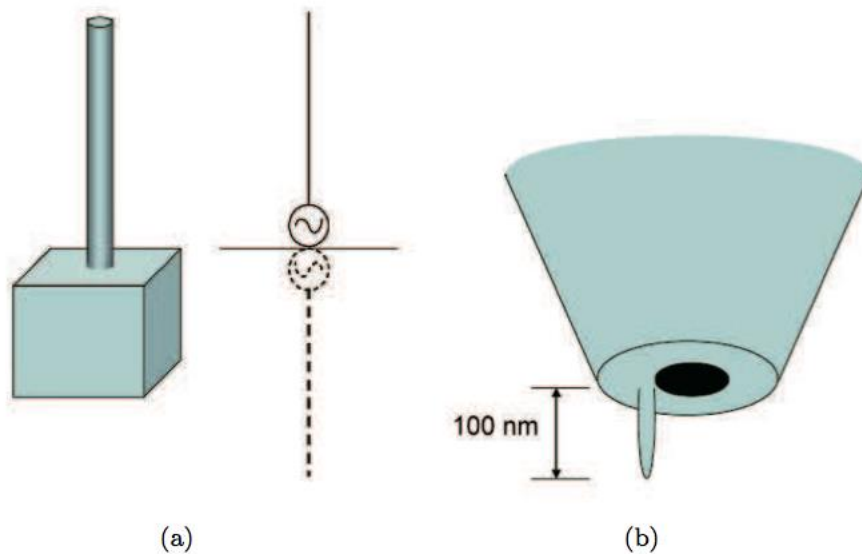


Figure 1- (a) A monopole antenna with ground plane functions as a dipole antenna and (b) a monopole antenna on the tip of a NSOM[2]

Many applications use this fact to their advantage; for example, a monopole antenna fabricated on the tip of a NSOM and gold or silver nanoparticle as dipole antenna on a tip of glass fiber used to detect fluorescence from single molecules demonstrating the use of

localized fields in the antenna[2, 3]. Hence, the optical antenna is defined as a device designed to efficiently convert free-propagating optical radiation to localized energy and vice-versa.

This demonstrates the capabilities of optical antennas in detecting electromagnetic energy well below the diffraction limit and with very high spatial resolution. Thus, optical antennas have a natural application in microscopy and high resolution imaging.”

As discussed earlier, due to the electron plasma oscillations on the metal surface, all previous efforts based on optical dipole antenna in conjunction with rectifying diode (in combination called “optical rectenna”) produced very low IR to electrical conversion efficiencies ($< 1\%$) This is also a result of low antenna IR absorption cross-section[4-8]. Previous attempt on nanostructured metal IR bolometer resulted in very low peak responsivity of 3 V/W where detection limit (D^*) and temporal response were not reported in the study possibly due to low absorption and higher noise floor[9].

1.3 Proposed two-element optical antenna array IR detector

The excitation of surface plasmons at optical frequencies on metal surfaces is unavoidable due to the inherent lattice structures of metals. The question is can we use this loss for the detection of IR radiation? To accomplish that first the key scientific challenge will be to artificially increase the plasma loss so that 100% incident IR radiation is absorbed. Second, a mechanism needs to be devised which can sense the loss in order to detect the IR radiation without adding extra noise. In this thesis, we study a two-element optical antenna array comprised of a perforated metallic (gold) hole array coupled with an underneath disk

array which functions as a “light funnel” to trap incident radiation as dipole currents. The sub-wavelength hole-disk antenna array when attached with a ground plane results in strong extraordinary transmission [10-12] through the hole array and zero back reflection. The energy is dissipated as electron plasma loss on the hole-disk system inducing perfect ~100% absorption of the incident radiation. This extraordinary absorption originates from simultaneous zero crossing of real component of permittivity and permeability due to the geometrical arrangement of the two antenna elements which nullifies overall charge and current distributions, prohibiting existence of any propagating electromagnetic modes at resonance. Further, the absorption band is shown to tune over entire mid-IR band by tuning dipolar coupling between two antenna elements by changing element dimensions or array spacing. The continuous perforated film allows probing of the induced “micro-current” plasma loss on each nano hole-disk via a weak bias current. Other optical antenna array designs primarily based on sub-wavelength discrete nanostructures demonstrate tight field confinement, but lacks overall high absorption as well as direct detection option due to discrete nature of the design[3, 13-15]. The proposed concept nicely combines discreteness and continuity requirements via radiative coupling between two elements taking advantage of both tight field localization of discrete disk array and direct detection ability of the continuous perforated film. Further development of simple nanoimprint lithography based large area optical antenna array fabrication technique facilitates formation of low cost point detectors for spectroscopic detection as well as high-resolution dense focal plane arrays for “color” IR imaging.

2. FREQUENCY SELECTIVE OPTICAL ANTENNA ARRAY ABSORBERS

The proposed optical antenna array consists of three parts- a perforated metal film coupled to its matching hole array and the hole-disk array brought in close proximity to a thick metal plane acting as a mirror. To analyze this structure, its necessary to decouple the complex system analyze the constituting parts separately and then use this analysis to understand the structure as a whole. First section of this chapter focuses on the analysis of the first part, i.e., the transmission analysis of the perforated metal film coupled to a disk array and then it is verified experimentally in the second section. Third and fourth section elaborate on the dynamics of cavity coupled hole-disk array. The last section explains in detail about the various numerical techniques used throughout this chapter.

2.1 Analysis of Transmission Through Hole-Disk Antenna Array

Fig. 2 and 3a illustrate the proposed two-element perforated gold film coupled with the disk array. To analyze the complex interaction in the hole-disk array, we used a professional simulation program called CST Microwave Studio. Structure layout and dimensions used in electromagnetic simulations are shown in Fig. 2. Various parameters shown in the figure are - period, diameter, relief depth and top metal thickness, which are labeled as P, D, RD and T respectively. Also, the hole shape is modeled as a rounded square (with radius of 270nm) in simulations to closely correspond to experimental results. Dispersion of gold was obtained by fitting Palik's experimental data with Drude model, and

refractive index of SU8 is considered as 1.55. S parameters of the structure were calculated and reflection was obtained as S_{11}^2 .

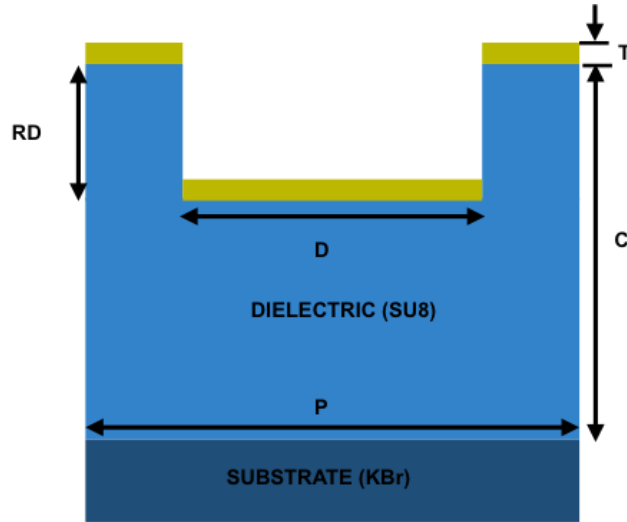


Figure 2- Structure cross section showing fabrication parameters

The transmission predicted from CST simulations is very low over the 3-10 μm mid-IR band through the hole-array with diameter 0.76 μm , period 1.14 μm , and hole-disk separation (relief depth (RD)) of 74 nm as shown in Fig. 3b. We can see total transmission 10% through the 45nm thick gold film with hole-array mainly due to extraordinary transmission as compared to just a plain gold film, through which the transmission is less than 1%. However, after the addition of a disk-array below the hole-array, a strong $\sim 50\%$ transmission peak appears around $\lambda = 4.53 \mu\text{m}$, as can be seen in Fig. 3b. The high transmission through this hole-disk coupled system originates from a different transmission mechanism compared to the extraordinary transmission through a simple

sub-wavelength metallic hole. The cross-sectional electric field distribution in Fig. 3c shows strong vertical hole-disk and lateral disk-disk coupling at the peak wavelength of transmission. By placing the perforated film on top of the disk-array, weakly transmitted electric field in 3-6 μm wavelength range for the present example (Fig. 3b) excites dipolar localized surface plasmon resonance (LSPR) on the disks. The localized charges on the edges of the disks attract opposite charges on the corresponding edges of the matching hole and adjacent disks in the lateral direction as observed from the field distribution shown in Fig. 3c. Due to strong coupling between disk-disk and hole-disk pairs, the coupled system functions as an optical antenna and transmits more energy than just a perforated metallic film.

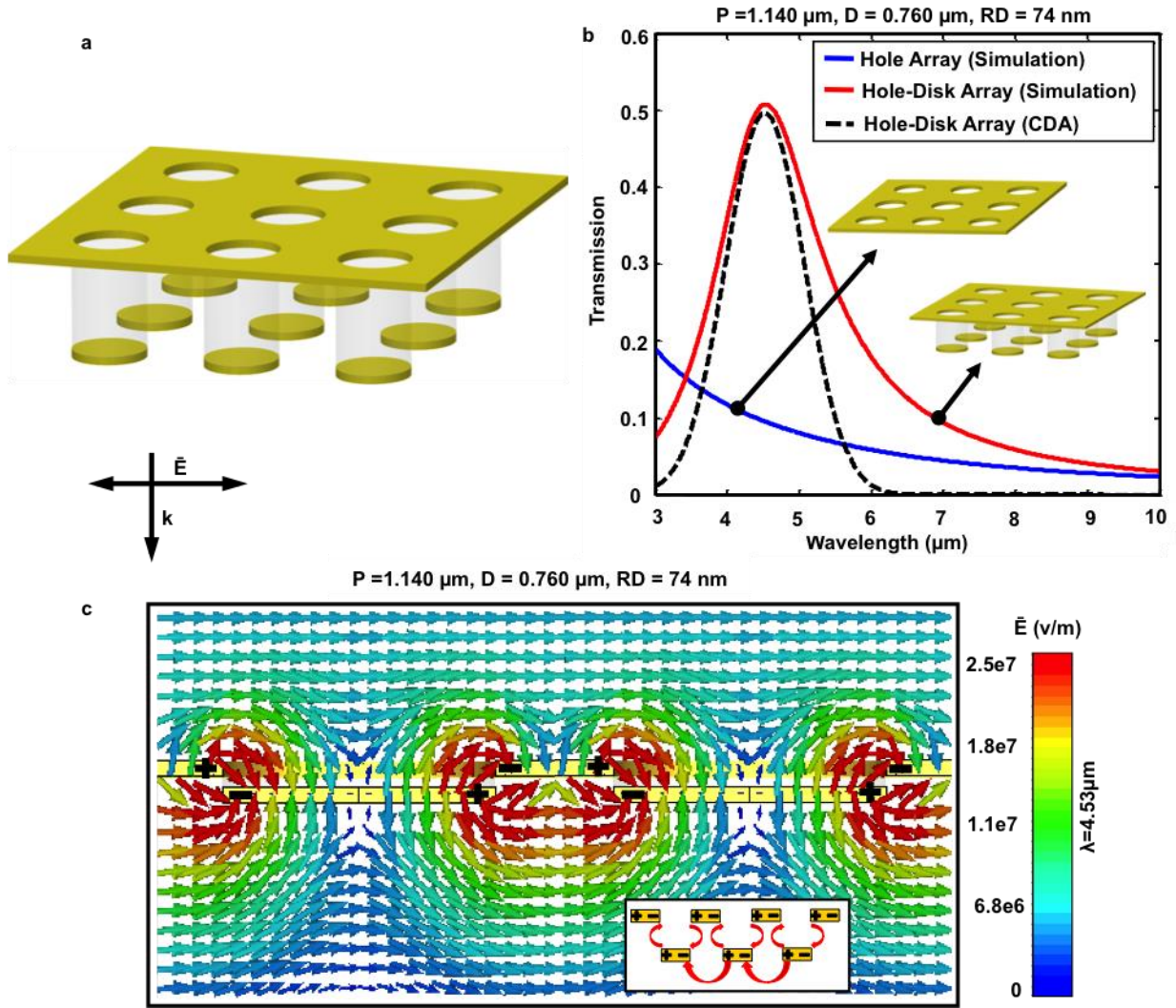


Figure 3- (a) Structure layout of hole array coupled with complementary disc array, (b) Transmission calculated from electromagnetic simulation of just the hole (blue), coupled hole-disk array (red) compared to that of theoretical CDA model(black) and (c) electric field distribution in the coupled hole-disk array structure

The electric field radiation from an oscillating electric dipole is given by[16]

$$\vec{E} = \frac{1}{4\pi\epsilon} \left\{ \frac{\omega^2}{c^2 r} (\hat{r} \times \vec{p}) \times \hat{r} + \left(\frac{1}{r^3} - \frac{i\omega}{cr^2} \right) [3\hat{r}(\hat{r} \cdot \vec{p}) - \vec{p}] \right\} e^{i\omega r/c}, \quad (1)$$

where \vec{p} is the electric dipole, ω is its angular frequency and r is the distance between the dipole and point of observation. According to this relation, the electric field radiation from the disk array is more than that from perforated film because the electric dipole moment of the disk is larger than that of hole at resonance due to the higher charge concentration and higher lifetime of localized surface plasmons present on the disks. As a result of dipolar charge oscillations, the disk array reradiates a part of this energy in all directions. On the upper side, most of the energy is reflected back from the hole-array, as its transmission is low. So the energy is mostly radiated in the downward direction.

To understand the coupling mechanism between the hole array and disk array, a modified Coupled Dipole Approximation (CDA) approach in conjunction with calculation of reflection/transmission through a multi-layer stack is followed[17, 18]. In this approach, the coupling between hole-disk and disk-disk dipoles mediated by near field and far field radiation can be calculated using Eq. (1). To further understand the relation between this coupling mechanism and the extraordinary transmission of the hole-disk array, one needs to study the behavior of disk and hole arrays independently. Hole-disk combination forms a complementary system and the transmission through the hole is equal to the reflection from disk array[19]. The polarizability (α) and the lattice contribution (S) of the circular disk array are used to estimate reflection (r) and transmission (t) coefficients of the disk array. Subsequently, the reflection and transmission of the disk array is used to estimate the reflection and transmission of the hole array based on the approximate relation, $t_{\text{hole}}/r_{\text{hole}} = r_{\text{disk}}/t_{\text{dis}}$ [19]. The reflection/transmission coefficients of these independent hole

and disk system are used to develop the reflection and transmission coefficient of the combined hole-disk system based on Fresnel expression of the resultant multi-layer stack. The detailed derivation of CDA method is given in the last section of this chapter. The CDA predicted transmission of the coupled hole-disk system is plotted along with results from electromagnetic simulation in Fig. 3b. The CDA prediction matches numerical simulation closely, vindicating the validity of the analytical model.

The overall response of the system can be tuned by manipulating the coupling between hole-disk and disk-disk pairs. By changing the relief depth (RD), two different regimes in hole-disk coupling are observed- first a blue and then red shift of the transmission peak as a function of increase in RD. Fig. 4a shows this relation for a constant period, $P = 1.140 \mu\text{m}$ and diameter, $D = 0.760 \mu\text{m}$ (which ensures constant disk-disk coupling). To understand this behavior it is necessary to identify different force interactions in the system. Firstly, there is a coupling between hole and disc, which is required for generation of strong charge oscillations on the corresponding disc, and then there is disc-disc coupling which increases the re-radiation efficiency. These coupling forces interact with each other to in a manner such that if either one of them dominates, the overall transmission reduced. This indicates that there exists an optimal value of RD where these coupling forces interact with each other to produce maximum transmission for the structure. This is a critical point (R^{D_c}), at which phase transition occurs in hole-disk coupling. If RD is decreased below R^{D_c} , hole-disc coupling is much stronger than the disc-disc coupling and it resists the restoring force responsible for charge oscillations on the disc, which results in slower charge oscillation

effectively red shift the transmission wavelength and reducing the transmission amplitude.

On the other hand, if RD is further increased from RD_c , charge oscillations induced on the disc are much weaker resulting in reduced transmission as well as a red shift in the transmission wavelength.

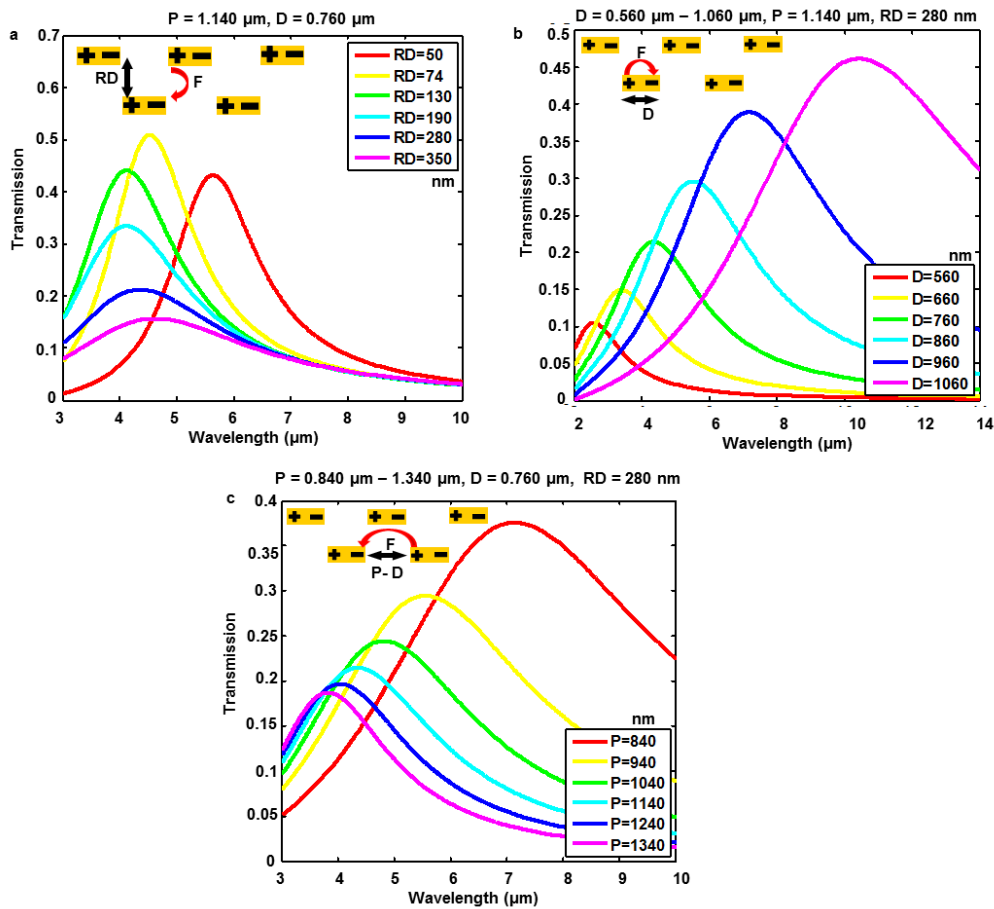


Figure 4- (a) Transmission of the hole-disk array for different RD.(b) different diameters (with constant period.) and (c) different periods (with constant diameter.)

For a constant hole-disk coupling (constant RD), the transmission peak location can be tuned over a wide range by manipulating disk-disk coupling by changing the diameter and

period of the system. For this study, a relatively large $RD = 280$ nm is used for the ease of actual fabrication of this structure at a later stage because a small RD increases the possibility of destroying the isolation between the hole and disk system during metal deposition. To understand the reason behind this tunability, we should revisit Eq 1. It says that $|\vec{p}| = qd$, where, p is electric dipole moment, d is the distance between the charges (which is approximately equal to the diameter) and charge q , which depends on the electric field strength and the diameter of disk. As the LSPR wavelength on the disk is inversely proportional to the diameter, an expected red shift is observed with increase in hole/disk diameter for a constant period as observed in Fig. 4b. Also, for the same case, it can be seen that as the hole diameter is increased, the electric dipole gets stronger and as a result, the transmission is enhanced as well. The LSP field enhancement on the edges of the hole/disk parallel to the excitation polarization is higher than other locations due to the charge accumulation along the field. Now consider a case where disk diameter is kept constant and period is varied keeping all other parameters constant. As the period increases, the distance between elements also increases, and hence, the opposite electric fields on the elements that originate from neighboring localized charges, decrease. As a result, the effective restoring force is relatively stronger which increases the charge oscillations blue shifting the transmission peak. It means that the effective electric field on the surface and consequently the effective spring constant, k_{eff} increases which results in a blue shift in the spectrum, as shown in Fig. 4c

2.2 Hole-Disk Antenna Array –Fabrication Process, Results and Discussion

The hole-disk antenna array was fabricated following a simple large area nano-imprint technology. First, a large area master pattern (4mmx4mm) with desired surface features is written with techniques like electron beam lithography or deep UV lithography. Then a polydimethylsiloxane (PDMS, 10:1 Sylgard 184) replica (or a stamp) of the master pattern is created which has inverse surface pattern compared to that of the master pattern. A thin layer (870nm) of SU8 2000.5 was spin-coated on a KBr substrate (4 mm thick), as the substrate needs to be transparent in infrared regime for transmission measurements. The PDMS stamp is then embossed on SU8 layer creating surface relief pattern same as the master pattern. Finally, a thin layer of gold (~45) is deposited with electron beam evaporation process on this imprinted pattern completing the fabrication process. It is this final layer of gold that forms the hole-disk array under study and the dielectric layer is there for mere mechanical support. A step-by-step visual guide for the fabrication process is shown in Fig 5.

Transmission spectra were collected using a 2.5X, 0.07 numerical aperture IR transparent KBr objective lens on an optical microscope (Hyperion 1000) coupled to a Fourier transform infrared spectrometer (Vertex 80) and outfitted with a spatial aperture having a diameter of 3.75 mm.

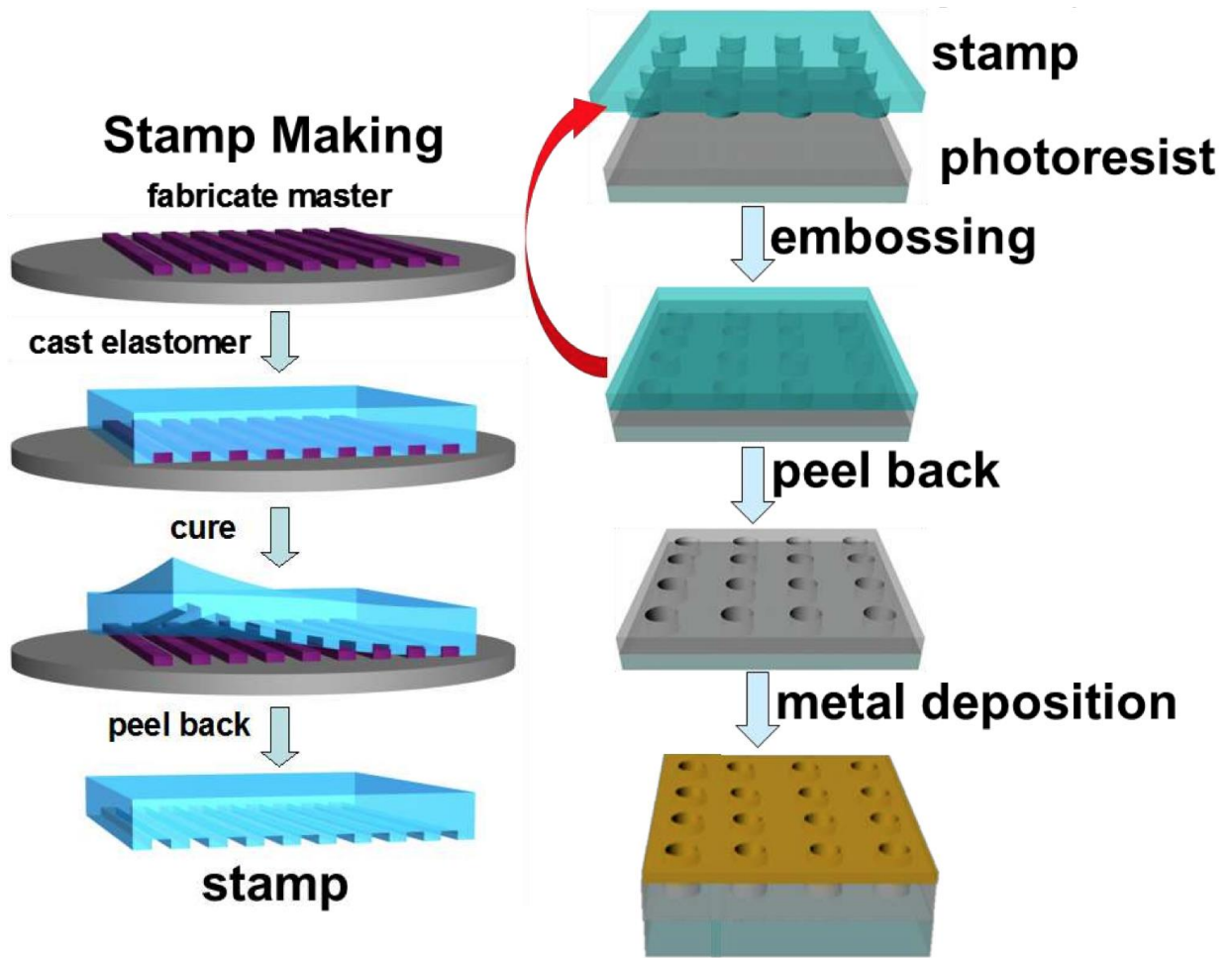


Figure 5- Step by step fabrication process of the hole-disk array

From Fig.6a it can be seen that, experimental and simulation spectra match with each other very well. The slight mismatch in the amplitude is due to the fact that RD for fabricated samples is less than that used for simulation (280nm). The control of RD is an issue as the applied pressure on the mold while imprinting varies from sample to sample unless the process is automated which can guarantee the exactness of the imprinted dimensions.

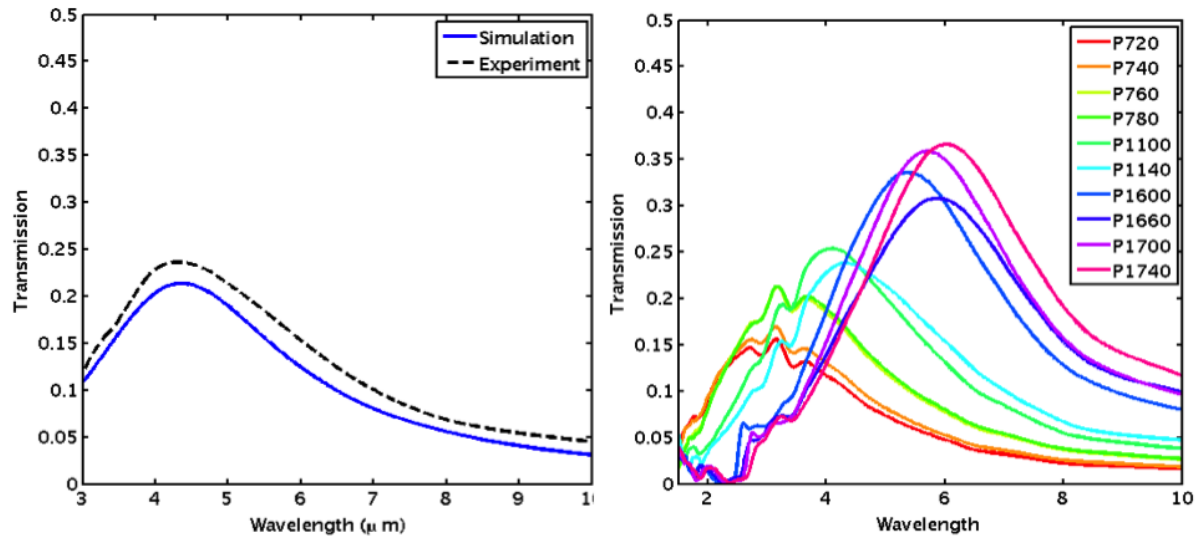


Figure 6- a) Simulated and measured transmission spectrum for Period $1.14 \mu\text{m}$ and Diameter $0.76 \mu\text{m}$. The slight mismatch in amplitude is due to the RD of experimental sample being smaller than targeted 280nm , which was used for simulation and (b) Experimental transmission spectra as a function of increasing period.

Fig.6b shows the spectra for different values of periods (720-1740nm) keeping D/P ratio constant (~ 0.66). There is a clear trend of linear increase in transmission wavelength as the diameter is increased. Detailed discussion of this behavior of the hole-disk array and its use in creation of a perfect absorber will be discussed in the next section.

2.3 Cavity Coupled Hole-Disk Antenna Array

This section will describe the dynamics of hole-disk array coupled to a cavity with the help of simulation and an analytical mode. In the last section, an analytical model of the system is developed with the CDA method. The schematic diagram of the structure under study is given below.

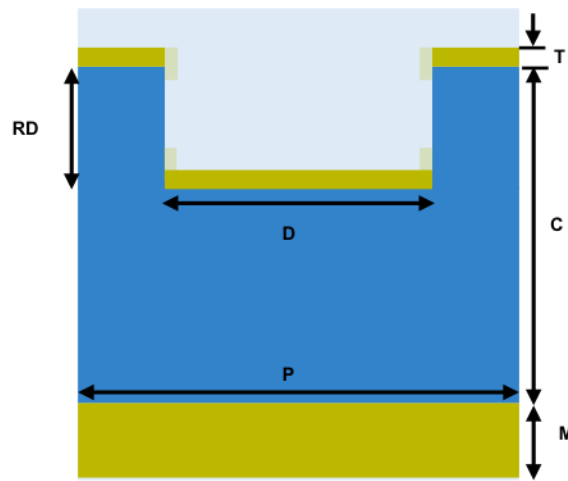


Figure 7- Schematic diagram of the structure under study

The interaction between the two-element hole-disk system and incident electromagnetic wave is further enhanced by addition of a mirror forming an optical cavity as illustrated in Fig. 7 and 8a. The enhanced electric field excites stronger electric dipoles on the hole/disk, which results in zero reflection and enhanced extraordinary transmission through the hole/disk system resulting in 100% absorption as electron plasma loss as shown in Fig. 8b. The narrow bandwidth of this absorption originates from the narrow cavity phase relation based on the Q of the cavity. The transmission through the bare hole-disk system is plotted along with the absorption in the cavity-coupled case in Fig. 8b to demonstrate this spectral

narrowing effect. Further, to understand the fundamental physics behind the cavity coupling mechanism with the hole-disk optical antenna, the CDA method is used to model these interactions accurately and the analytical CDA prediction is overlaid on top of the simulated absorption result in Fig. 8b. The close correspondence between simulation and CDA predictions validates the analytical model. The corresponding electric field distribution predicted from simulation at the resonance is shown in Fig. 8c. It can be observed that the lateral coupling between disk-disk is enhanced by more than one order of magnitude in presence of the cavity (compare Fig. 4c). In a same manner as described for the bare hole-disk system, the absorption peak location can also be tuned by changing period and diameter of the system.

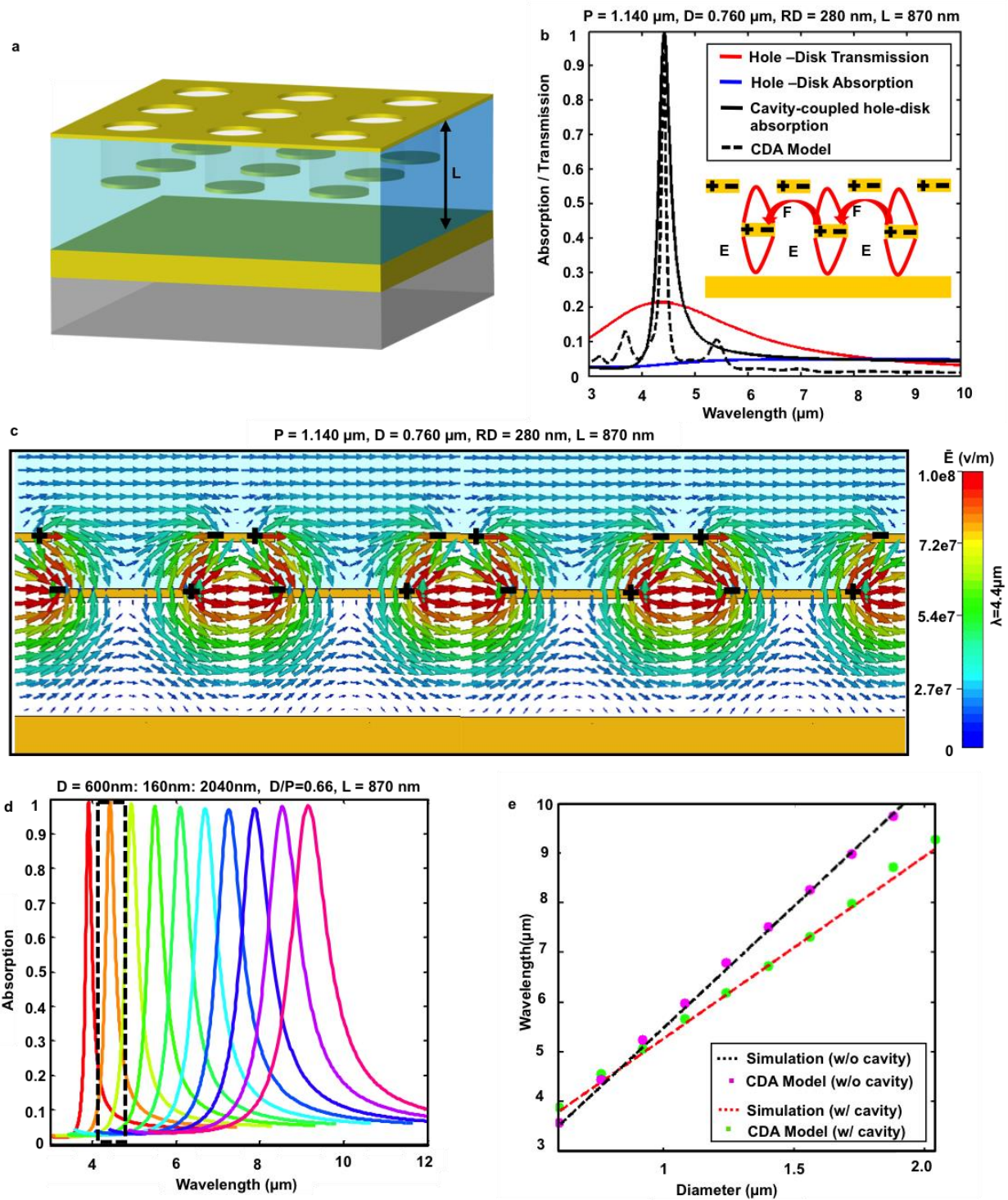


Figure 8- (a) Cavity coupled hole-disc array 3D schematic, (b) Comparison of simulation and CDA spectra for this structure, (c) Electric field profile at the

resonance wavelength, (d) Tunability of absorption peak as diameter is scaled keeping D/P ratio = 0.66 and (e) Comparison of simulation and CDA method in locating peak positions of hole-disc array with and without cavity coupling

Fig. 8d shows the absorption spectra as a function of increase in hole/disk diameter for a constant $D/P = 0.66$ (corresponding bare hole-disk system transmission is shown in Fig. 9).

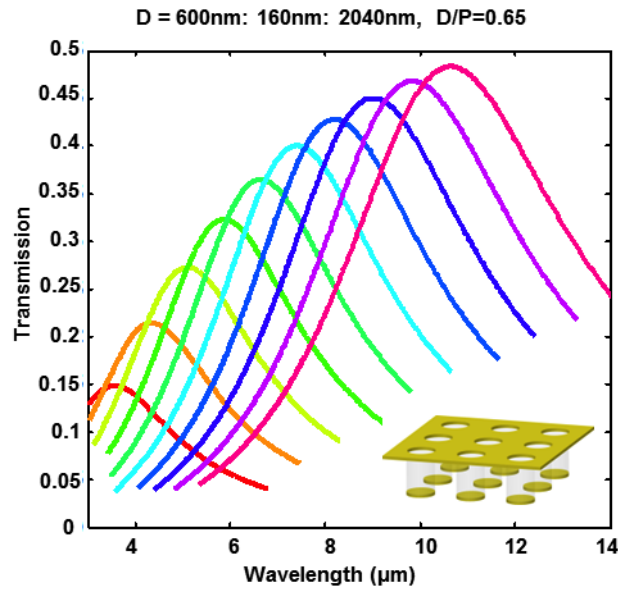


Figure 9- Transmission of the hole-disk array for different diameter ($D/P = 0.66$ is kept constant)

As discussed previously, the LSPR in hole-disk system red and blue shifts by increasing diameter and period, respectively. Changing diameter/period changes the resonance wavelength in an implicit manner. A closed form expression that relates period with effective spring constant doesn't exist for 2D array due to complexities in multi-modal and multi-dimensional interactions. However, the LSP resonance frequency depends on the

diameter explicitly as, $\omega_{res} \propto \frac{1}{D}$. Hence, the resonance frequency is more sensitive to diameter changes. The transmission and absorption peaks of the structures with and without the cavity as a function of diameter between 600 nm and 2.040 μm for the constant $D/P = 0.66$ and constant cavity thickness $L = 870$ nm is computed using both CDA and CST simulation have been plotted in Fig. 8e. A very close correspondence between simulation and CDA model can be observed in predicting the absorption band location. From Fig. 8e it can be observed that the wavelength shift for the cavity coupled case lags behind the bare hole-disk system due to extra phase accumulation inside the cavity.

Accumulation of phase at different interfaces inside the cavity plays an important role in cavity-induced absorption in the structure. Based on the coupled-dipole approximation, we establish the condition for the maximum absorption: the excitation of localized surface plasmon resonance should overlap with the Fabry-Perot mode inside the cavity. This effect can be seen at its strongest when the disk is placed at the quarter wave position. The Fabry-Perot mode inside the cavity enhances the electric field on the disk array when it is placed at the position of quarter wave where the incident and reflecting field are in phase on the disk surface. As a result, constructive interference between two counter propagating waves excites a strong electric dipole on the disk. Additionally, cavity coupled absorption is stronger in the wavelength region which overlaps with the LSPR bandwidth. The simulated absorption spectrum as a function of cavity length and wavelength is shown in Fig. 10a for the hole-disk system having $P = 1.140$ μm , $D = 0.760$ μm , $RD = 280$ nm. The predicted first

order Fabry-Perot mode ($L = \frac{\lambda}{2n_{eff}}$) corresponding to a simple planer cavity has been plotted on top of the CST simulation data in Fig. 10a. A clear deviation in resonance of the hole-disk cavity system from the simple FP resonance is evident due to the extra phase shift acquired by the cavity mode in presence of the disk at the localized surface plasmon resonance. This extra phase shift ($\Delta\phi$) makes the effective thickness of the cavity larger which shifts the resonance to a higher wavelength. To quantify this effect, the phase lag from the disk array is calculated with CDA approach and it was used to perturb the ideal cavity phase relation which resulted in shift in the cavity resonance as can be seen in Fig. 10a (left). As expected there is a $\pi/2$ phase lag between the dipole oscillator and incident wave[20] (Fig. 10a (left)) at the LSPR wavelength (Fig. 10a (right)). Away from the plasmon resonance, the extra phase shift approaches the steady state phase due to the change in index in presence of the metallic disk array inside the cavity. The predicted resonance peak shift ($\Delta\lambda$) of the cavity-coupled hole-disk array with respect to the planer Fabry-Perot resonance for the first mode ($m = 1$) calculated by CDA and electromagnetic simulation is plotted in Fig. 10b. The close match between CDA and simulation vindicates the analytical phase approximation of the CDA approach. According to Fig. 10a, for low cavity thicknesses, the Fabry-Perot resonance peak falls within LSPR bandwidth of the hole-disk arrays. In addition, for these thicknesses, for the chosen relief depth ($RD = 280$ nm), the disk array satisfies the quarter wave condition. As a result, the system fulfills all conditions to maximize the electric field on the disk array and consequently the absorption is maximized in this region. At higher cavity thicknesses, these three conditions do not satisfy

simultaneously and hence the absorption goes down. However, higher order modes ($m = 2$ and $m = 3$) of the cavity satisfies all of these three conditions over the chosen cavity thickness range resulting in high absorption over the entire range.

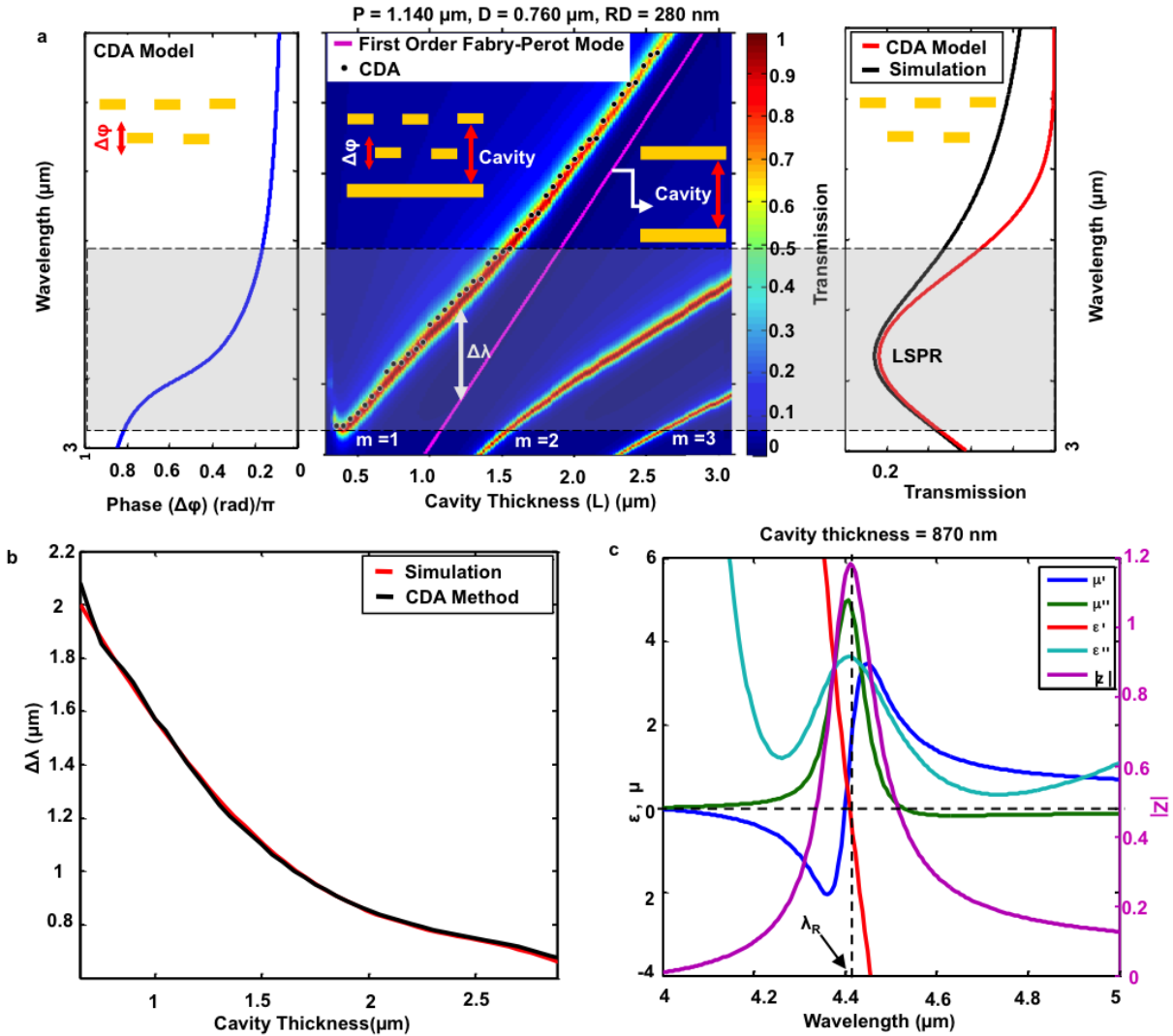


Figure 10- (a) (left) Phase shift in cavity mode due to LSPR, (middle) Cavity mode vs. the actual structure absorption as a function of cavity thickness, (right) Transmission from the hole-disk array, (b) Change in cavity resonance position ($\Delta\lambda$) as a function of cavity thickness and (c) Extracted effective refractive index at $C=870\text{nm}$.

To further investigate the absorption mechanism, effective refractive indices of the system are extracted following standard method of inversion of Fresnel transmission and reflection coefficients[21, 22]. The extracted indices for the cavity geometry having $P = 1.140 \mu\text{m}$, $D = 0.760 \mu\text{m}$, $RD = 280 \text{ nm}$, $L = 870 \text{ nm}$ (the corresponding absorption peak has been marked with dotted box in Fig. 8d) has been plotted in Fig. 9c for an x-linearly polarized excitation. It can be observed that at the resonance wavelength $\lambda_R \approx 4.41 \text{ mm}$, both real component of permittivity (ϵ') and permeability (μ') crosses the zero indicating absence of electric and magnetic polarizability of the multi-layer structure at resonance.

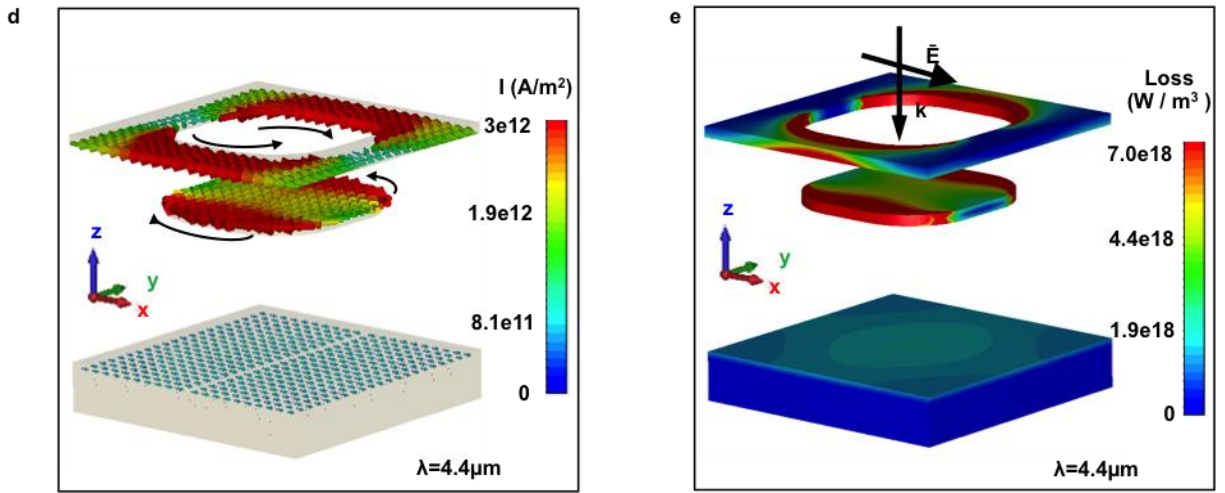


Figure 11- (a) Current density and (b) Power loss density in the structure at the resonance wavelength of 4.41 μm .

The simulated current distribution in Fig. 11a at resonance shows that the currents on holes and disk oppose each other canceling overall charge distribution. It means that the total magnetic induction, which is the response of the structure to the incident electromagnetic field, is zero. So, the effective permeability of the whole structure at the

resonance frequency is also zero. However, imaginary components of both permittivity (ϵ'') and permeability (μ'') are non-zero at resonance indicating loss due to excitation of currents on hole and disk surfaces. The loss component of the permittivity at resonance originates from the excitation of LSPR and the permeability resonance stems from the opposite edge currents on hole and disks that forms a magnetic dipole, which interacts with the magnetic field of the incident EM wave. Fig. 11b shows the loss profile of the system where it can be observed that the complete loss takes place on the edges of the hole-disk system indicating primary location of interaction. The transmitted electric field through holes excites LSP on disks, which moves towards four corners of the element perpendicular to the polarization direction due to the two-dimensional lateral coupling between disks. LSP's on disks in turn excite opposite charges on the edges of holes and the amount of this interaction depends on the radiative field strength of the disks, which is proportional to the distance between disk and hole arrays. As a result, there are two counter propagating dipole currents on the edges of the disks and holes (Fig. 11a). These opposite current densities make two magnetic dipoles on two opposite sides of the hole and disks, which are localized on the edges. According to $P = \vec{J} \cdot \vec{E}$, loss happens because of these current densities, where \hat{J} is the current density; \vec{E} is the electric field and P is the loss power density. Fig. 12a schematically illustrates the electric (\vec{F}_E) and magnetic (\vec{F}_B) forces, which play role in drifting current along y-axis towards the edges on the disk.

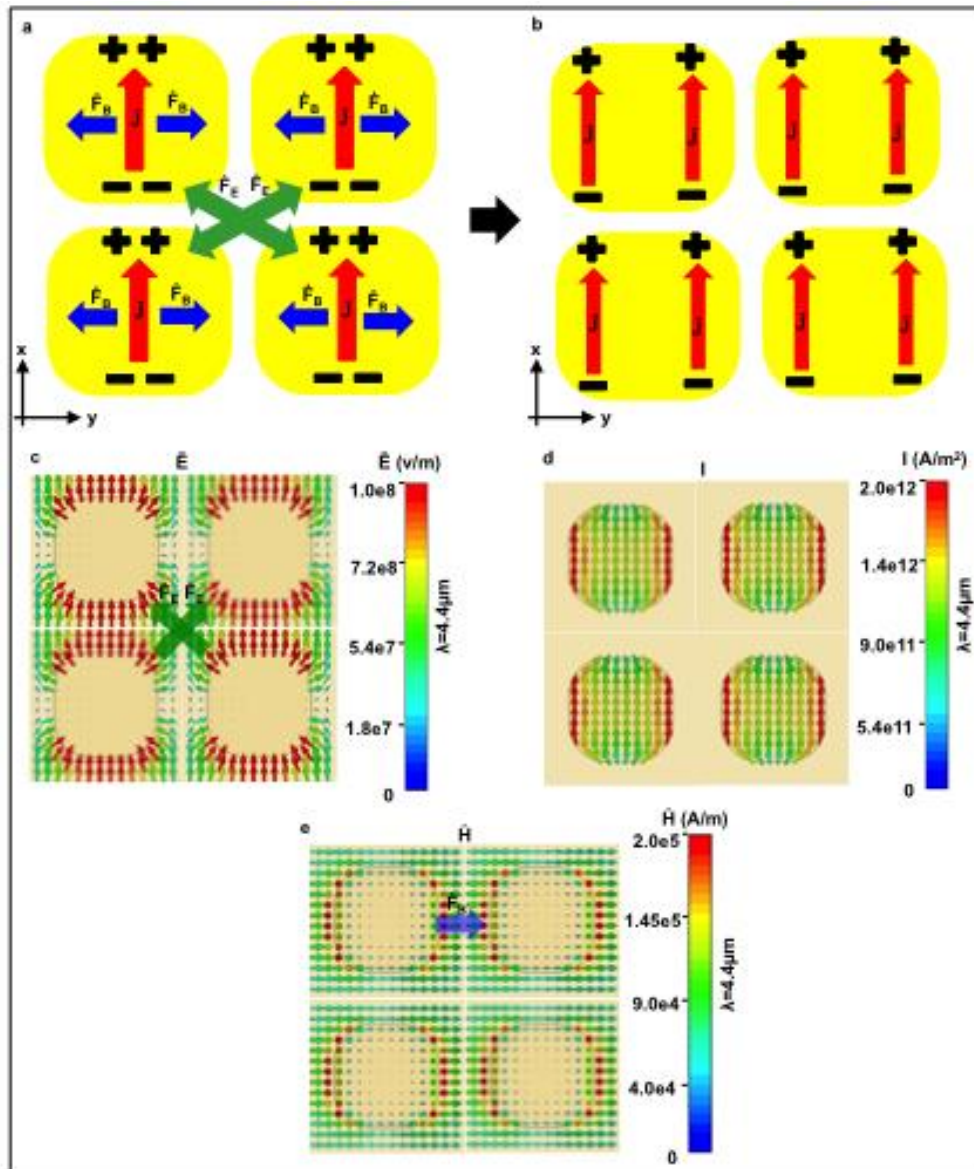


Figure 12- Loss processes in the cavity-coupled hole-disk system.

The electromagnetic simulation verifies the presence of these electric and magnetic forces in Fig. 12c and Fig. 12e respectively, resulting in separation of current along y-axis as shown schematically in Fig. 12b and Fig. 12d. The 3D current distribution calculated from

simulation is shown in Fig. 11a. It clearly shows the origin of the loss on the edges of the hole-disk as demonstrated from simulation in Fig. 11b.

2.4 Cavity Coupled Hole-Disk Antenna Array –Results and Discussion -

The fabrication technique used in this case is same as hole-disc array with the only difference of substrate. Instead of using KBr window, a glass substrate with a thick layer (200nm) of gold is used for spin coating the resist. Other steps for fabrication of the sample are same as before.

Fig. 13a shows the scanning electron microscope (SEM) images of 5 such representative systems with varied hole/disk diameter for $D/P \bar{\Gamma}$ (0.60-0.66). The corresponding optical absorption measurements using a microscope-coupled FTIR (Bruker Inc., Hyperion 1000-Vertex 80) along with simulation predictions appear in Fig. 13b. As predicted, about 100% absorption of the incident radiation can be observed. The relation between absorption peak location and hole/disk diameter is plotted in Fig. 13c both for experimental measurement and simulation. The previously predicted linear relation between the resonance location and the hole/disk diameter is observed in experimental measurements as well. Slight variation can be observed in absorption peak location, which is a result of D/P ratio for different structures not being exactly same.

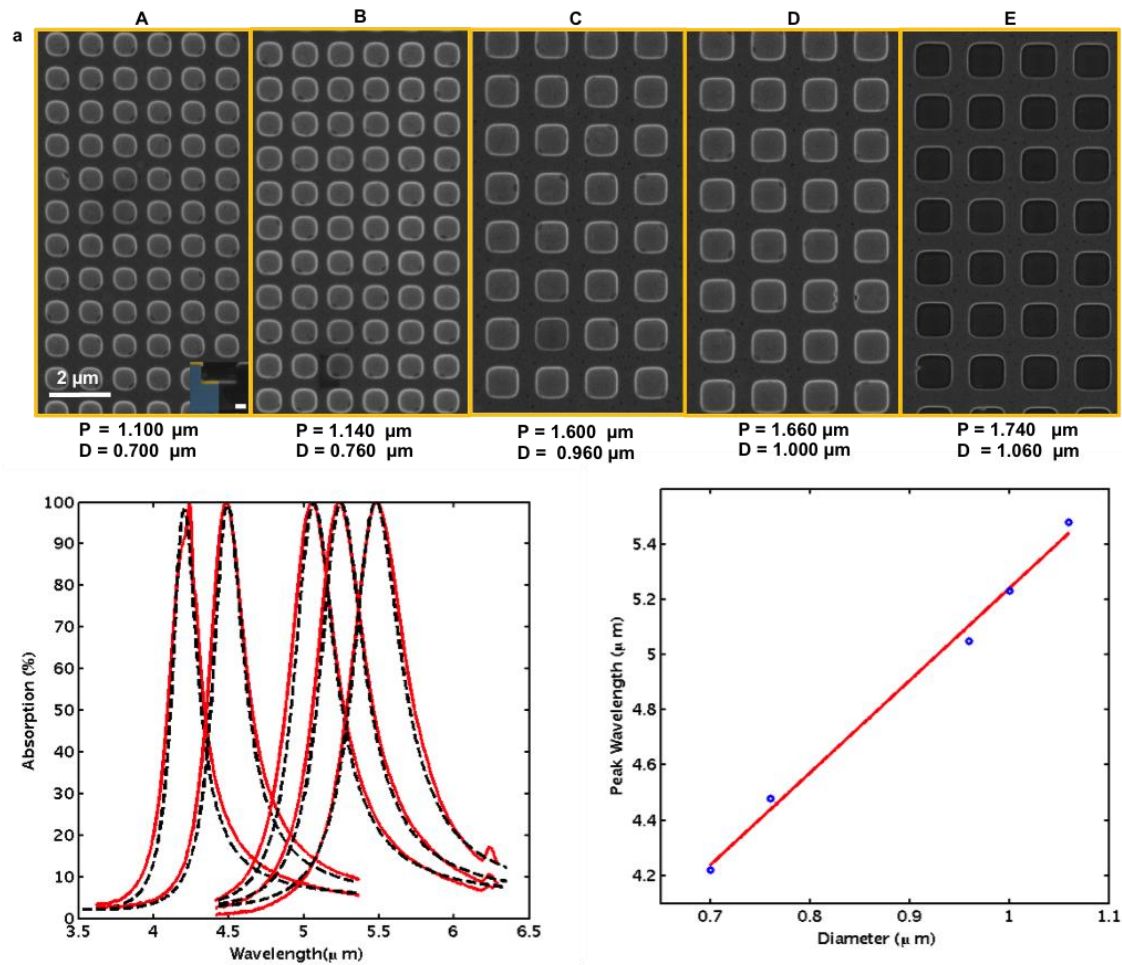


Figure 13- (a) SEM image showing the hole-disk pattern with 5 different periods, (b) corresponding simulated (black) and measured (red) absorption spectra and (c) peak location as a function of diameter for these structures

The two-element optical antenna system demonstrates an interesting mechanism to enhance extraordinary transmission. The strong dipolar coupling between two elements enhances the transmission/absorption to $\sim 100\%$ when coupled with an optical cavity. The coupling between two elements can be varied flexibly to shift the resonance location and strength. Tunability can also be exploited from the cavity phase relation, which can be

simply tuned with cavity thickness. Such controlled infrared absorption when implemented in conjunction with simple large area imprinting techniques[23] will lead to development of a newer classes of infrared sensors.

2.5 Numerical Methods

In this section, various numerical and mathematical methods that are used in previous sections are described in detail.

2.5.1 Modified Coupled Dipole Approximation (CDA) Method –

This section describes the Coupled Dipole Approximation method used throughout this chapter to analyze the hole-disk antenna array with and without cavity coupling. To outline CDA approach, first, it is necessary to calculate the polarizability of a single disk in presence of dipolar LSPR. This polarizability is then used to calculate the effective polarizability of the entire disk array. This effective polarizability is then used to calculate the transmission and reflection coefficients of the disk array. Then Babinet's principle, which states that the reflection/transmission from a disk array is actually transmission/reflection from a hole array, can be used to find the reflection/transmission from the hole array. Lastly, the response of the composite system can be determined using Fresnel's equations treating the system to be formed of multiple layers of different materials with known values of reflection and transmission. Detailed mathematical treatment is given below-

Firstly, polarizability of the array is calculated as:

$$\alpha_{cluster} = \frac{\alpha_s}{1 - \alpha_s S}, \quad (2)$$

where α_s is the is the polarizability for a single disk and S is lattice contribution to the polarizability, which can be calculated as-

$$S = \sum_{j \neq i} \left[\frac{(1 - ikr_{ij})(3 \cos^2 \theta_{ij} - 1)e^{ikr_{ij}}}{r_{ij}^3} + \frac{k^2 \sin^2 \theta_{ij} e^{ikr_{ij}}}{r_{ij}} \right]. \quad (3)$$

Polarizability of a disc can be calculated from the polarizability of a generalized ellipsoidal nanoparticle, which is given by

$$\alpha_s = \varepsilon_0 V \frac{\varepsilon - \varepsilon_m}{\varepsilon + L_a (\varepsilon - \varepsilon_m)}, \quad (4)$$

where ε and ε_m are the dielectric function of the metal and surrounding medium, respectively, V is the volume and L_a is the shape factor of the ellipsoid which is defined as:

$$L_a = \frac{abc}{2} \int_0^\infty \frac{dq}{(a^2+q)\{(q+a^2)(q+b^2)(q+c^2)\}^{1/2}} \quad (5)$$

where a is the diameter of the ellipsoid along the polarization direction, b and c are the diameters along other two dimensions. The reflection coefficient of the disk array is

$$r_{disk} = \frac{\pm iG}{\alpha^{-1} - S}, \quad (6)$$

where

$$G = \frac{2\pi k}{A} \begin{cases} \cos^{-1} \theta, s - polarization \\ \cos \theta, p - polarization \end{cases},$$

k is the wavenumber and A is the area of unit cell. Positive and negative signs stand for s and p-polarization respectively. The transmission coefficient of this disk array is

$t_{disk} = 1 \pm r_{disk}$. The reflection and transmission of the disk array is used to estimate the reflection and transmission of the hole array based on the approximate relation-

$$\begin{cases} r_{hole} = t_{disk} \\ t_{hole} = r_{disk} \end{cases}. \quad (7)$$

The reflection and transmission coefficients of a thin layer on top of a substrate, are estimated as

$$r_{tot} = r + \frac{(1 \pm r)^2 r_s e^{2i\beta}}{1 - r_s r e^{2i\beta}} \quad (8)$$

and

$$t_{tot} = \frac{(1 \pm r) t_s}{1 - r_s r e^{2i\beta}} \quad (9)$$

In these equations, positive and negative signs stand for s and p-polarization. r is the reflection coefficient of the thin film. r_s and t_s are reflection and transmission coefficients of the substrate. In addition, β is the propagation phase in the thin-film

$$\beta = \beta_r + i\beta_i = \sqrt{\varepsilon_{spacer}} k_0 d. \quad (10)$$

To obtain hole-disk system transmission analytically, Eq. (2)-(7) was used following the multiple reflection formula Eq. (8)-(10), we calculated the reflection and transmission of the system as:

$$r_{disk+hole} = r_h + \frac{(1 + r_h)^2 r_d e^{i(2nk_0 l_2)}}{1 - r_d r_h e^{i(2nk_0 l_2)}}, \quad (11)$$

$$t_{disk+hole} = \frac{(1 + r_h) t_d}{1 - r_d r_h e^{i(2nk_0 l_2)}}. \quad (12)$$

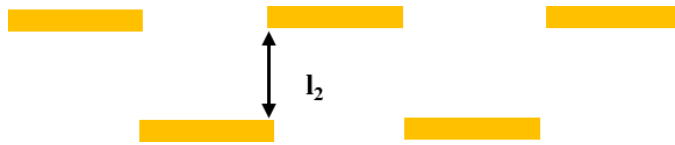


Figure 14- Hole- disk structure schematic diagram

In the CDA computation a large number of particles (1000) were considered in order to account for the far-field interaction between the holes and the disks. A very good agreement between the simulation and CDA model can be observed.

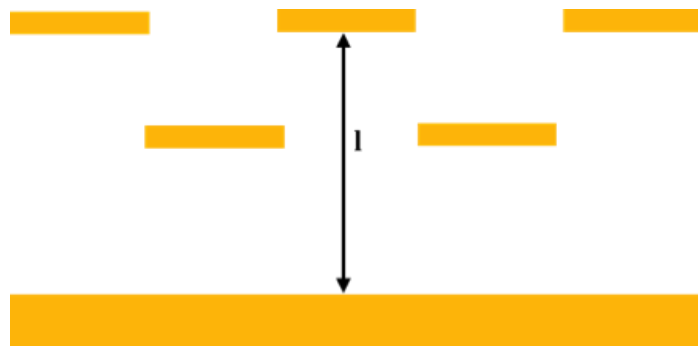


Figure 15- Cavity coupled hole-disk structure schematic diagram

In the cavity coupled case the hole-disk formulation is modified to account for the reflection from the back mirror and the round trip phase in Eq. (12).

$$r_{tot} = r_{Au} + \frac{(1 + r_{Au})^2 r_{disk+hole} e^{i(2n_{eff}k_0l)}}{1 - r_{disk+hole} r_{Au} e^{i(2n_{eff}k_0l)}}, \quad (13)$$

where l is the distance between gold back mirror and the top hole.

2.5.2 Effective Index Estimation

The effective index in Eq. (13) was calculated from Maxwell-Garnet theorem. The penetration of EM wave inside the gold is wavelength dependent. So, by using effective medium theory, we calculated effective refraction index of the spacer[24-27]. We considered different materials in z and r directions. To derive the effective refractive index, we divided the system into three regions as schematically shown below:

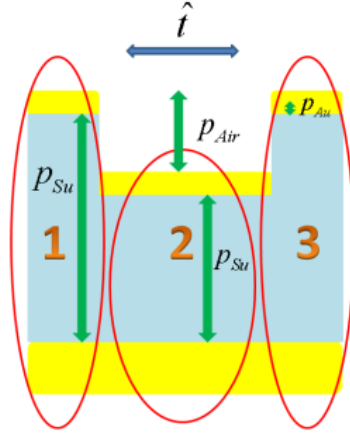


Figure 16- Separation of the structure for calculation of effective index calculation (i)

$$\langle D \rangle = \varepsilon_{eff} \langle E \rangle, \quad (14)$$

$$\varepsilon_{1eff} = \varepsilon_{3eff} = \frac{2 p_{Au} \varepsilon_{Au} + p_{Su} \varepsilon_{Su}}{2 p_{Au} + p_{Su}}, \quad (15)$$

and

$$\varepsilon_{2eff} = \frac{p_{Air} \varepsilon_{Air} + 2 p_{Au} \varepsilon_{Au} + p_{Su} \varepsilon_{Su}}{p_{Air} + 2 p_{Au} + p_{Su}}. \quad (16)$$

In these regions, because the polarization is parallel to the surface, so the electric fields in different regions are equal ($E_{1t} = E_{2t}$). In addition, p_{Au} is equal to skin depth of the gold.

Now three regions are defined by effective indices as illustrated below:

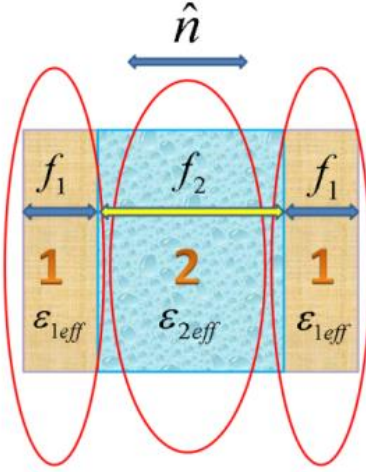


Figure 17- Separation of the structure for calculation of effective index calculation (ii)

The effective refractive index can be estimated by considering

$$D_{1n} = D_{2n} \quad (17)$$

$$\epsilon_{eff} = \frac{2 f_1 \epsilon_{1eff} E_1 + f_2 \epsilon_{2eff} E_2}{2 f_1 E_1 + f_2 E_2}, \quad (18)$$

Now, solving Eq. (17) and (18), one can derive the effective refraction index as

$$\epsilon_{eff} = \frac{2 f_1 + f_2}{\frac{2 f_1}{\epsilon_{1eff}} + \frac{f_2}{\epsilon_{2eff}}}. \quad (19)$$

In this coupled system also a good agreement between CDA and simulation can be observed.

2.5.3 Cavity Phase Evaluation

By using Eq. (6), we calculated the added phase (θ_{LSP}) of the transmitted electromagnetic wave according to the incident wave ($t = |t|e^{i\theta_{LSP}}$). After that by using Drude model for gold,

we calculated the phase of reflected waves, by using Fresnel equations ($r = \frac{\sqrt{\epsilon_{Au}} - \sqrt{\epsilon_{Su}}}{\sqrt{\epsilon_{Au}} + \sqrt{\epsilon_{Su}}}$);

Actually this phase is φ_{ref} ($r = |r|e^{i\varphi_{ref}}$) which is π for perfect conductors. Now, by adding

θ_{LSP} , φ_{ref} and the optical path length inside the cavity ($\gamma = 2(\frac{2\pi n_{su}}{\lambda})l_{su}$), we can calculate

the total phase which EM wave acquires inside the cavity. After that, by comparing this phase with the phase shift of a regular Fabri-Perot resonator, we obtained the effective thickness (l_{eff}) of the structure

$$(\varphi_{tot} = \theta_{LSP} + \varphi_{ref} + \gamma = \varphi_{ref} + 2(\frac{2\pi n_{eff}}{\lambda})l_{eff}). \quad (20)$$

2.5.4 LSPR vs. Diameter–

The LSPR resonance frequency depends on the force between localized charges

$$\omega_{res} \propto \sqrt{k}, \quad (21)$$

where, k is the spring constant given by

$$k = - \left. \frac{\partial F}{\partial x} \right|_{x=D}, \quad (22)$$

where F is the total coulomb force between positive and negative charges which depends on the number of separating charges (LSP's), N , and distance between them which approximately equals to diameter, D ,

$$F \propto \frac{N}{D^2}. \quad (23)$$

In 2D, the number of particles on the surface depends on D . Combining Eq. (21), (22) and (23) gives:

$$N_{2D} \propto D \Rightarrow \omega_{res} \propto \frac{1}{D}. \quad (24)$$

From Eq. (24) it can be concluded that the LSPR red shifts with the increase in diameter of the particle. This relation between diameter and resonance frequency is not exact, but it give us estimation for the behavior of this kind structures.

3. MULTISPECTRAL UNCOOLED INFRARED DETECTORS

From the previous section, we understood that incident radiation produces micro-currents on the hole-disk array and losses due to these currents are Ohmic in nature. As a result, there is a change in the temperature of the structure proportional to the intensity of the incident radiation. This phenomenon is same as the operational principle of bolometers and hence it was natural to explore the potential application of the structure as a bolometer.

Bolometers are a class of infrared detectors, which detect the presence of infrared radiation by changing its temperature dependent resistance. A schematic diagram of a general bolometer is shown in the figure below.

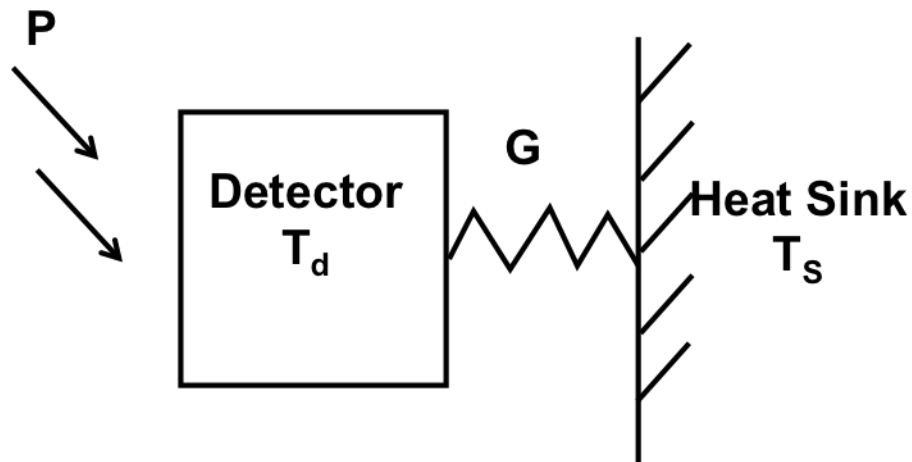


Figure 18- A schematic diagram of a basic bolometer

A bolometer consists of a detector element, a heat sink and a conductive element that connects the detector to the heat sink. The detector absorbs power P from the incident

radiation and loses some of it from the conductive link to the heat sink. This absorbed power changes the temperature of the bolometer from T_d to $T_d + \Delta T$, where $\Delta T = P/G$ [28]. The higher the incident power, the larger is the detector temperature change, which in turn translates to a linear resistance change. The detector responds to this increased temperature at a speed governed by its thermal time constant defined as $\tau = C/G$, where C is the thermal capacity of the detector and G is the thermal conductance of the link connecting detector to the heat sink. There is a built-in tradeoff associated with bolometer speed and a strong response. Very responsive devices have high C and low G (so, a high time constant) and are very slow to reset and fast devices have low C and high G (making the time constant smaller)[29]. To this date, bolometers remain a cheap, portable and comparatively, a moderate performance alternative to cooled semiconductor infrared detectors.

The possible application of the cavity-coupled nano antenna array as an infrared bolometer opens up new avenues for bolometer technology owing to the fine linewidth and tunability of the absorption peak. A possible interest would be creation of pixels tuned to different absorption wavelengths in infrared producing a color image similar to RGB in visible silicon detectors. The lack of any cooling systems makes the entire detector system less bulky and more portable.

To investigate this idea further, we first need to perform calculations predicting temperature change in the detector for a given amount of input power. For this purpose, multi-physics simulations are done to calculate the change in temperature of the structure.

The multi-physics simulations were run with CST Microwave studio in conjunction with CST MPhysics Studio. First, electric and magnetic fields, current densities and absorption losses from simulation model used in the previous section for the analysis of the cavity-coupled antenna array is imported in the CST MPhysics studio as ‘source elements’ for thermal modeling. Geometric parameters chosen for the simulation are period (P) = 1140nm, diameter (D) = 760nm, relief depth (RD) = 280nm, cavity thickness(C) = 870nm and upper metal thickness (T) = 45nm which makes sure that the absorption peak lies at $4.41\mu\text{m}$ within the atmospheric transmission window of $3\text{-}5\mu\text{m}$. The incident power is normalized as 5nW/unit cell ($1.2996\mu\text{m}^2$) and the background temperature is set to 300K. Temperature and thermal loss profile obtained from the simulation is shown in fig. 19.

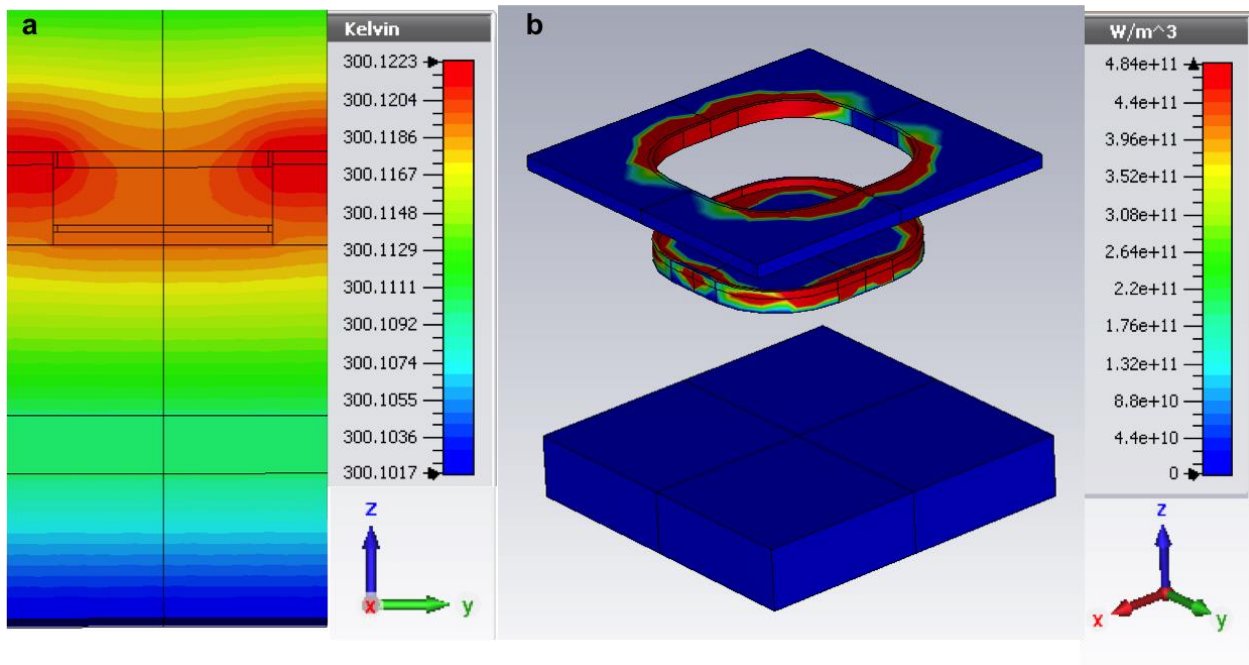


Figure 19- Simulations predicting temperature change and heat loss in the structure

It can be seen from fig. 19b that the thermal losses mostly take place on the upper layer and the disk and the temperature change (fig. 19a) is relatively high as well compared to other places in the structure. This localized temperature increase ($\Delta T \sim 0.12K$) causes the resistance of the upper film to change as a function of incident radiation.

3.1 Detector Pattern design, Master Pattern Writing and Fabrication

As mentioned in the previous chapter, the cavity-coupled antenna array was fabricated as a 4mm x 4mm continuous pattern. The resistance on the top surface is less than 1 Ohm and is not suitable for direct measurements of the detector's performance. So, the upper layer needs to be modified in such a way that the resistance goes up significantly[30]. To overcome these challenges, it was decided that after the imprinting step, there should be another UV lithography step where the upper layer is properly formatted prior to metal deposition. Fig. 20 shows the pattern used for making the lithography mask. The serpentine design makes sure that the base resistance of the detector is higher than sheet resistance. Simply changing the number of stripes or stripe width for the same pattern area can change the final resistance to a desired value.

For biasing the detector, a DC voltage is applied to a voltage divider circuit consisting of a resistor R1 and the detector Rd. The biasing circuit for the detector is shown in fig. 20b. Incident infrared radiation changes the detector resistance and it can be measured by monitoring the output voltage Vo that will indicate a change proportional to resistance change.

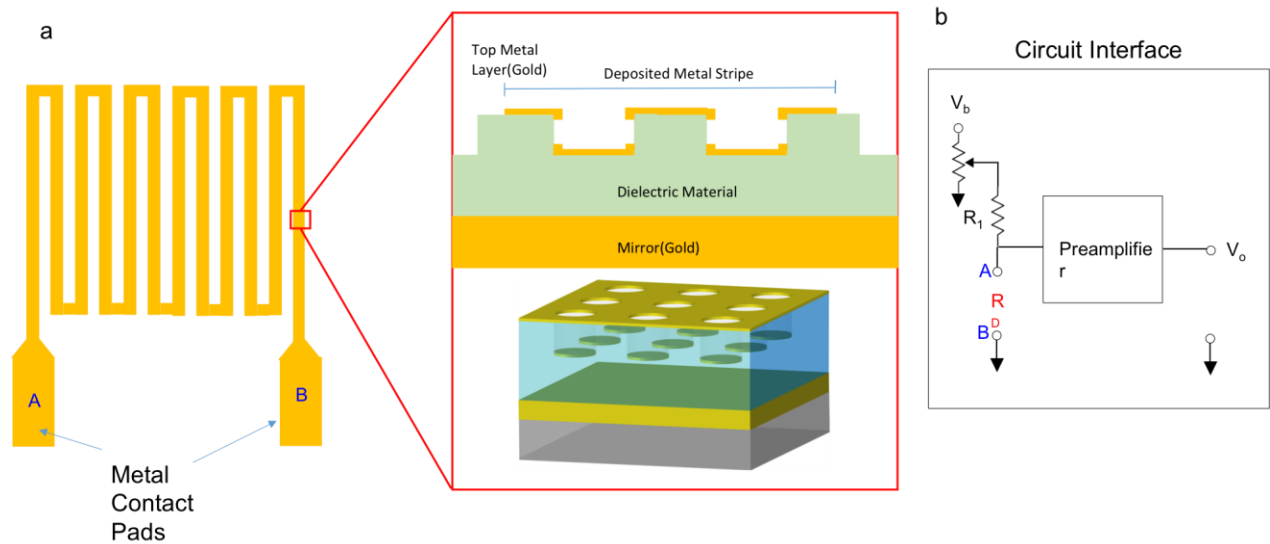


Figure 20- (a) A schematic diagram of the detector pattern and (b) biasing circuit of the detector

In the fabrication of the detector, there were two different master patterns used. In the first case, the previously used 4mm x 4mm master pattern was used for the imprinting process. This was done just to verify the proof-of-concept basic functionality of the detector even though there were issues like sometimes contact lines and pads ended up peeling off during liftoff and the sample resistance values being higher than predicted values, because in both cases hole-disk pattern was so large that contact lines and contact pads both ended up either on top of it or on the adjacent hole disk patterns with different periods.

The second master pattern is 1mm x 1mm in size and is written with a Nanoscribe 3D Laser Lithography system. The advantages over the previous approach are that the throughput of lift off process increased and the resistance values are much more consistent. Making the pattern smaller also helped in almost eliminating lattice defects which would occur in large patterns resulting in electrical open circuit.

Details of the master fabrication are given below-

Nanoscribe's Photonic Professional GT is a 3D laser lithography system is an analog of electron beam lithography system for writing comparatively larger structure sizes with minimum feature size on the order of hundreds of nanometers. The system consists of a sample holder mounted on dual stages – a piezo stage and an air stage and a 780nm femtosecond fiber laser with 120mW maximum power. The laser is focused on a photoresist-coated sample mounted on the sample holder on the piezo stage, which moves keeping the laser stationary to write the desired pattern. Piezo stage has a very fine accuracy of 10nm and can write patterns only upto 300umx300um in size. The air stage can span much larger area but has much smaller accuracy. A combination of piezo stage movement and air stage movement is used to write high-resolution large area structures.

With the laser lithography system, there are two ways in which we can write the master pattern. One way is to write it with negative resist, which means, writing a square mesh, which will form holes in the shape of rounded squares, and second way is to write with positive resist where the laser writes 'vacancies' on a spin-coated layer of resist on a glass substrate. Both methods have their own advantages and disadvantages for writing the coupled hole-disk arrays. For example, in negative resist method, the laser system will be actually writing a mesh as shown in the fig. 21a.

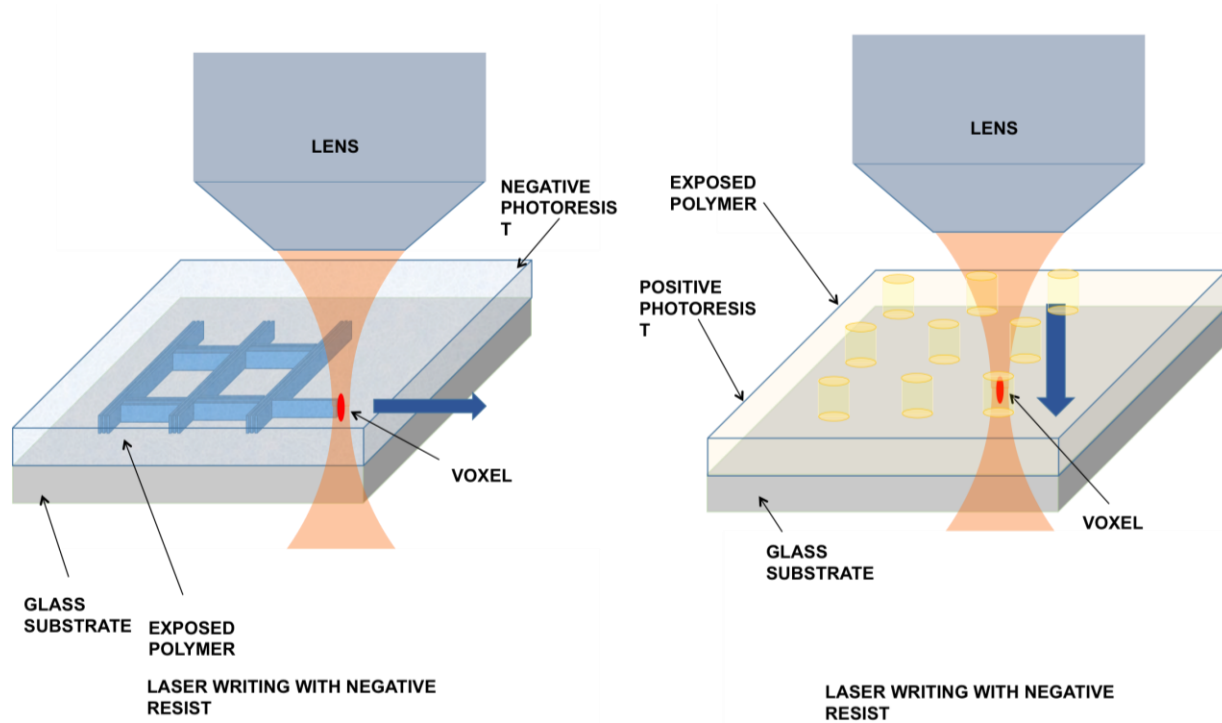


Figure 21- 3D Laser writing process (a) with negative photoresist and (b) with positive photoresist.

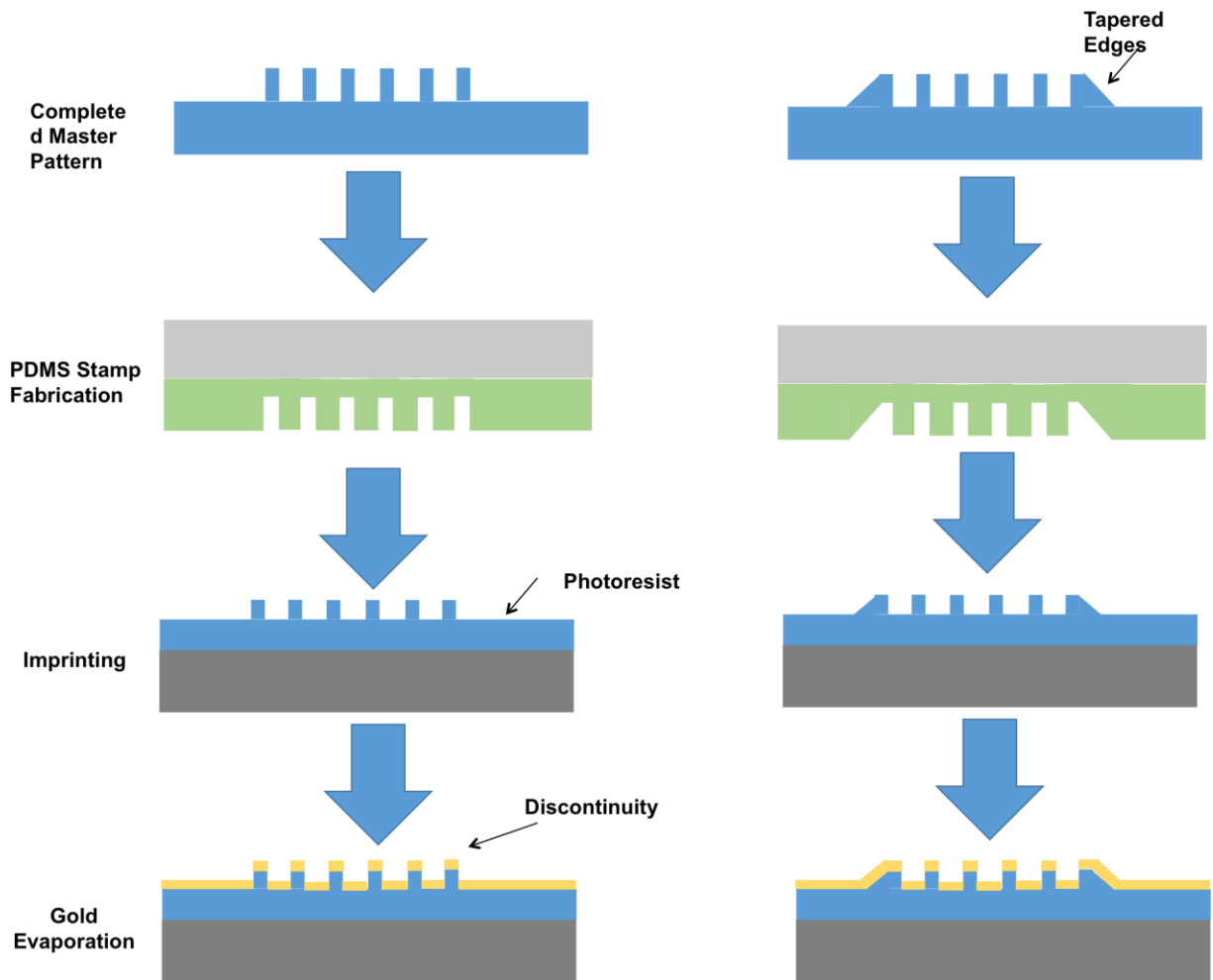


Figure 22- Step by step description of the nanoimprint lithography process

This method is fast and produces accurate hole shapes but it has associated disadvantages- first, the relief depth is not consistent for longer lines. This is a limitation on the substrate's angle correction mechanism where the substrate's actual inclination on the sample holder is not exactly determined by the system and at long distances from the start point, the laser eventually writes inside or over the substrate instead of writing at the interface of substrate and resist. The second disadvantage is electrical discontinuity at the pattern edges. This is pictorially depicted in fig. 22. The electrical discontinuity problem can be

overcome by writing a wedge shaped pattern around the boundaries of pattern but again this reduces the fill factor of the entire pattern by introducing additional vacant area between the smaller pattern pixels decreasing the sample absorption.

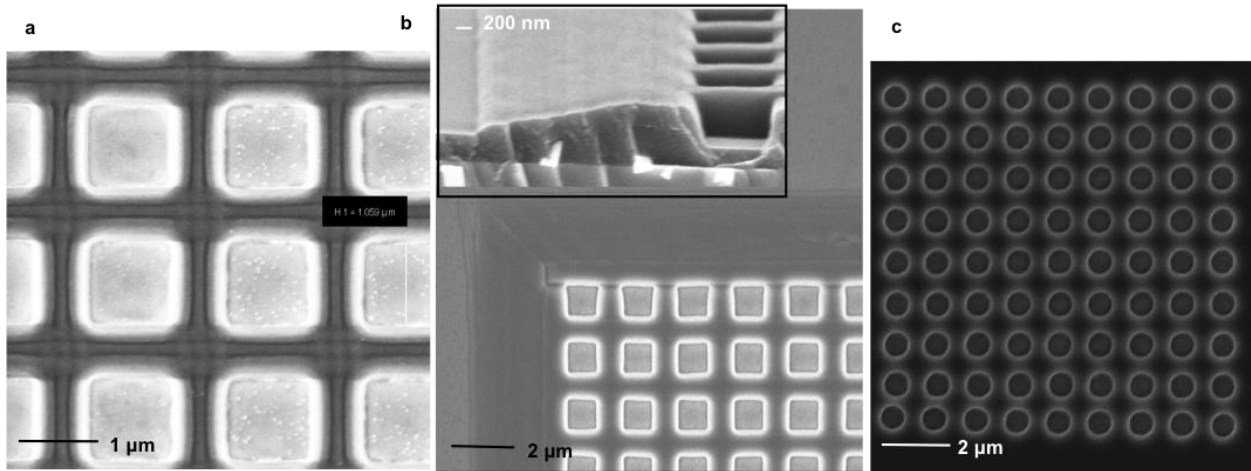


Figure 23- SEM images of the master pattern written with negative resist (a) top view, (b) cross section showing the tapered pattern and the tapered portion around the edges of a pixel and (c) master pattern written with positive resist

Second way is to write with positive resist. In this case, the laser writes vertical lines, which eventually become holes in the spin coated layer of positive resist after development. The advantage of writing with this method is that the relief depth of the structure is very accurate as it is defined by the spin-coating process, but is also much slower than writing with negative resist. This is pictorially shown in fig. 21b. Also, SEM image of the pattern written with this method is shown in fig. 23c.

Details of the sample fabrication process are given below-

1. A 200nm thick layer of gold is evaporated on a glass substrate with electron beam evaporation.

2. A thin layer of SU8 (800nm) is spin-coated on the gold mirror and is imprinted upon by the hole-disk array PDMS stamp.
3. After the imprint, the structure is UV exposed for 30 min. and baked for 30 min. after the exposure. This step is necessary to make the SU8 layer resistant to acetone lift off during the final stages of fabrication process.
4. The hard baked SU8 imprint is then processed with a UV lithography step with NR9 resist, where the hole-disk structure is patterned with serpentine pattern mask. This step makes sure that during metal evaporation, gold lands only on the serpentine pattern creating a high resistance conductive path on over the hole-disk layer.

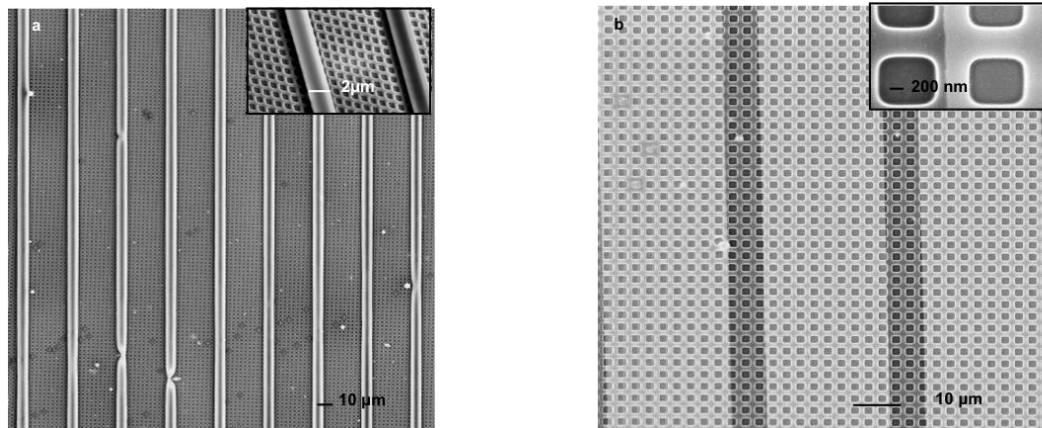


Figure 24 SEM images showing the detector sample (a) during photolithography step and (b) after metallization and lift off.

5. 45nm of gold is then evaporated on the sample and then excess gold and resist is then removed with acetone sonication. At this point, it is necessary that only NR9 is removed leaving SU8 unaltered, as the entire detector pattern rests on SU8.

A completely fabricated detector pattern is shown in fig. 24b and fig. 25.

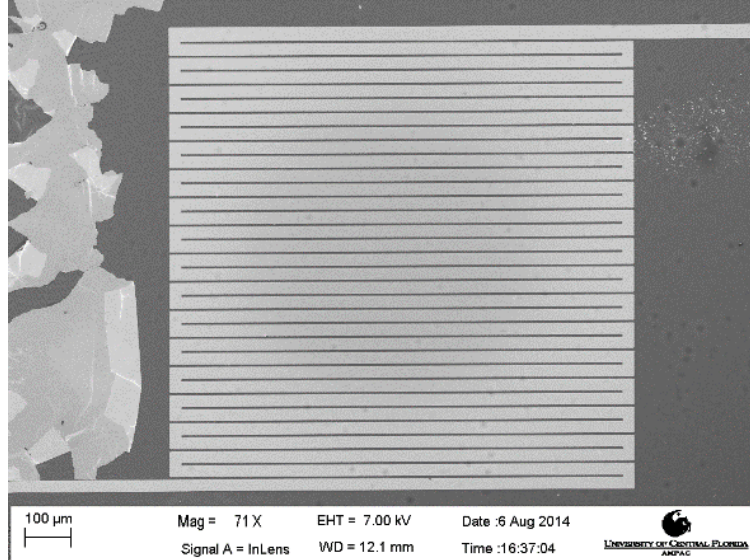


Figure 25- A SEM image of fabricated detector pattern.

3.2 Measuring Detector Performance Parameters

This section describes measurement setup for the detector samples, estimated performance parameters and the measured parameters. An infrared detector can be characterized on the basis of three parameters – responsivity (R), detectivity (D^*) and time constant (τ). Responsivity tells us how well a detector responds to the incident radiation and is measured in units of (Volts/Watt). Detectivity D^* is a measure of the noise performance of the detector and is described as [31]

$$D^* = \sqrt{A} * \frac{R}{S_n} \left(\frac{cm \sqrt{Hz}}{Watts} \right) \quad (25)$$

where A is the detector area and S_n is the noise spectral density measured in $Watts/\sqrt{Hz}$. Lastly, the time constant is the measure of how fast a detector responds to the incident radiation and is defined as $\tau = C/G$ measured in seconds, where C is the heat capacity and G is the thermal conductance of the detector. The apparatus used for detector characterization is shown in fig. 26. The detector is mounted in front of a black body source (Infrared Systems, IR-564) with temperature range of 50s-1200°C and is DC biased with a voltage divider circuit as shown in fig. 20. Radiation from the black body is chopped with an optical chopper with frequency range of 0-400Hz. The detector generates an AC signal proportional to the intensity of this chopped radiation, which is superimposed on top of the DC output of the voltage divider circuit. An AC coupled amplifier circuit (Infrared Systems,) with adjustable gain from 250-1500 and a bandwidth of 0.15Hz to 15kHz decouples the AC detector response from the voltage divider output. The output of the amplifier circuit is fed to lock-in amplifier (Stanford Research Systems SR830) and spectrum analyzer (Stanford Research Systems SR760), which communicate with a PC with Matlab over RS232 bus.

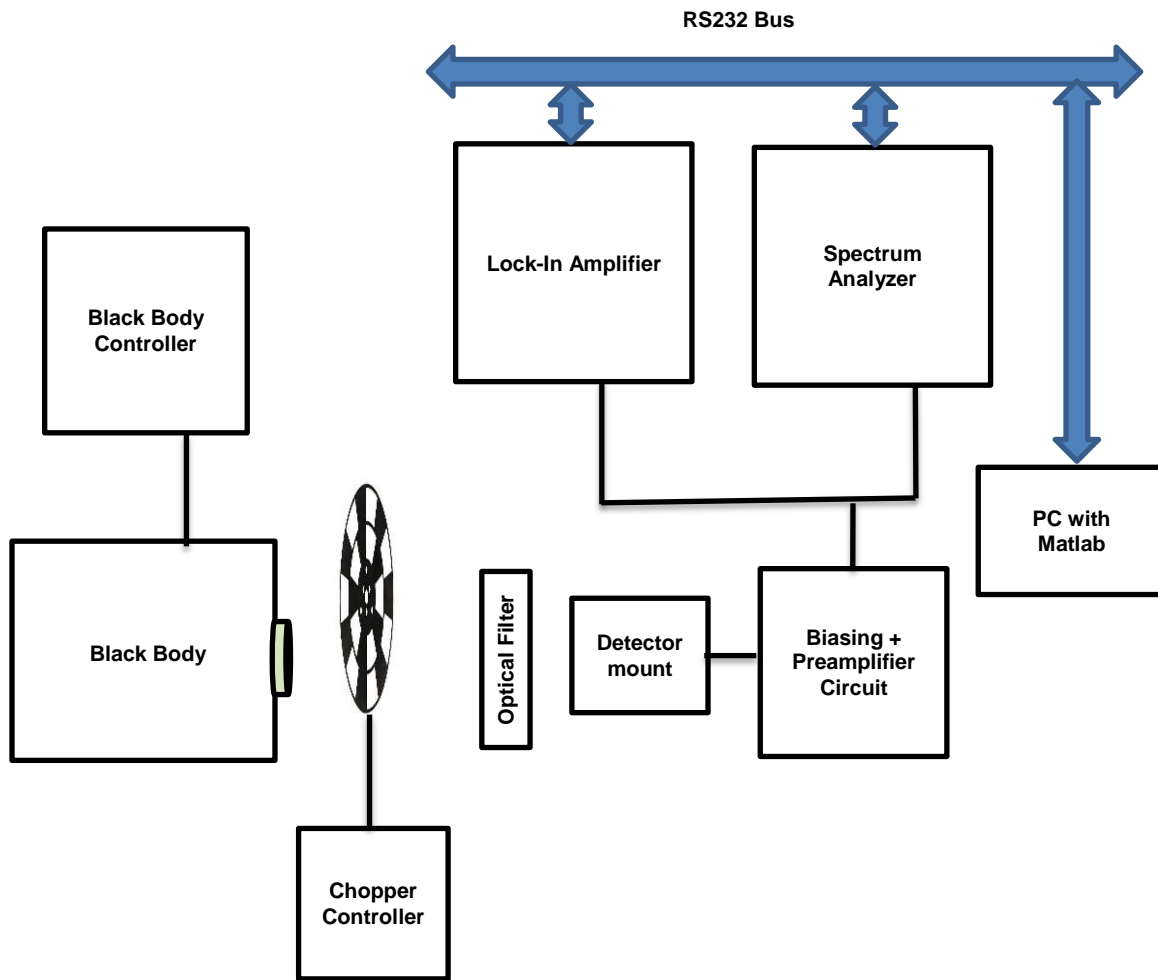


Figure 26- A schematic diagram of the setup used for characterization of the bolometer

An image of the detector mount is shown in fig. 27. A high conductance silver epoxy was used to connect wires to the contact pads of the detector, as the resist layer under the metal does not permit for good quality wire bonding.

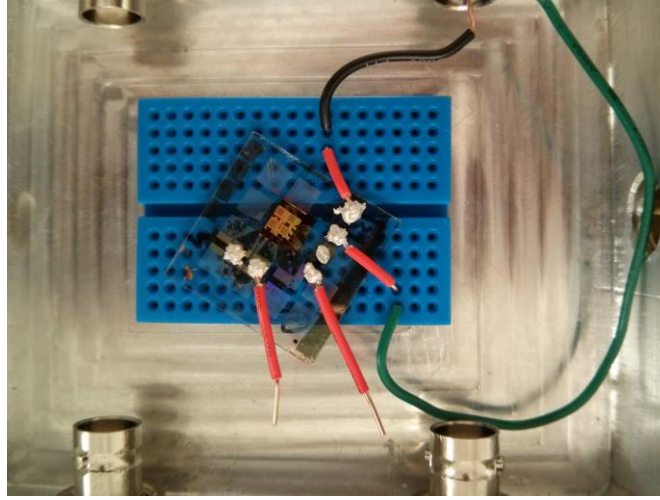


Figure 27- An optical image of the fabricated detector sample. Electrical connections are made to the sample with a low resistance silver adhesive.

To calculate different performance parameters of the detector, we first need to know how much power is absorbed by the detector for different temperatures, blackbody aperture sizes and geometry of the measurement setup. For this calculation, the black body temperature is recorded and then the blackbody spectrum is multiplied with optical filter transmission spectrum and sample absorption spectrum. The integration of this curve gives us radiance of the black body source for a particular temperature that is actually absorbed by the sample. These spectra and their product are plotted in fig. 28.

Mathematically, it can be represented as-

$$L^*(T) = \int_0^{\infty} \frac{2hc^2}{\lambda^5(e^{hc/\lambda kT} - 1)} A(\lambda)F(\lambda)d\lambda \left[\frac{W}{cm^2 sr} \right], \quad (26)$$

Where, L^* is the radiance of the source that is absorbed by the sample, A is the absorption spectrum of the sample and F is the transmission spectrum of 3-5 μm filter used for measurements.

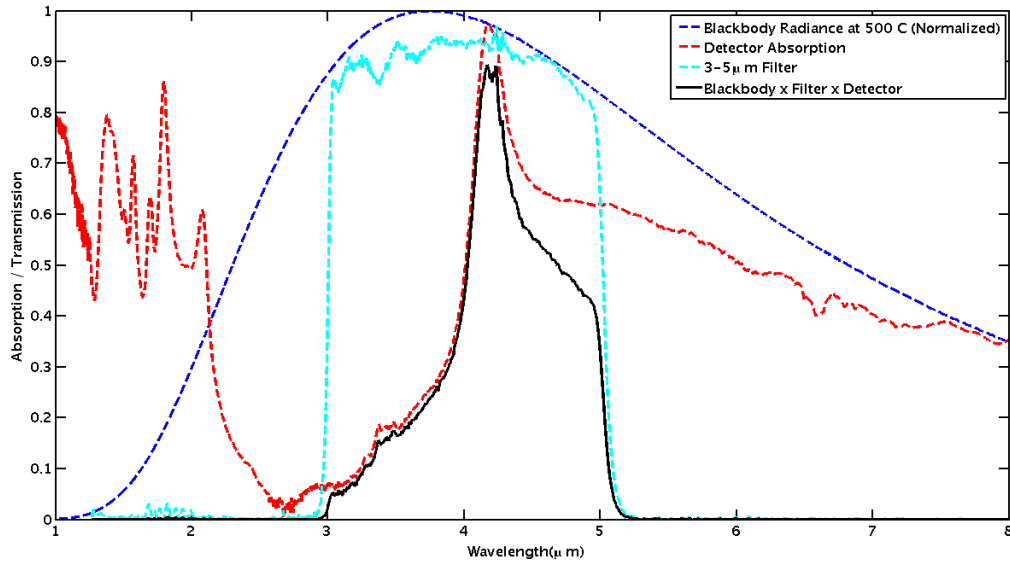


Figure 28- Various spectra used in the calculation of incident power on the sample.

After calculating the source radiance L^* , power incident on the sample can be calculated as

$$P = L^* A_s \Omega_d, \quad (27)$$

Where, A_s is the source area and Ω_d is the solid angle subtended by the detector at the source. This incident power along with the noise spectral density from the detector is then used to calculate responsivity R and specific detectivity D^* .

One of the important performance parameters of a bolometer is its noise equivalent power (NEP), which is used in calculation of D^* . It is defined as the incident power necessary to produce an output signal equal to noise signal. It is measured as

$$NEP = \frac{S_n}{R} \quad (28)$$

where S_n is the noise spectral density and R is the responsivity. The total noise in the bolometer is a sum of noise from all the noise processes superimposed on each other. The noise mechanisms are-

1. Johnson-Nyquist noise- Also known as the white noise and thermal noise is present in electronic circuits due to thermal agitation/ random Brownian motion of the electrons. This noise is constant over the entire frequency spectrum and hence it is also known by the name- 'white noise'. Its calculated as

$$v_{RMS} = \sqrt{4k_B TR \Delta f} \quad (29)$$

2. Phonon Noise- Phonon noise arises due to the heat exchange between the bolometer and its surroundings like substrate and atmosphere. This noise is present even in thermal equilibrium and causes temperature fluctuations in the detector. When the bias voltage is increased, both Johnson and phonon noise goes up as a result of Joule heating. It is calculated as –

$$P = \sqrt{4k_B T^2 G} \quad (30)$$

3. Photon noise- a radiation source emits photons, which are a result of several internal processes varying with time. This makes the number of photons emitted by the source fluctuate about an average number, giving rise to photon noise.
4. 1/f noise – This is also known by the names of flicker noise and pink noise. This noise power has 1/f frequency dependence and has equal power in every octave.

This means for same amount of noise power at high frequency, the noise spectral density decreases but the bandwidth increases.

5. Lastly, electronic measurement components also contribute towards the measured noise according to their specifications.

For noise measurements, output of the amplifier circuit is connected to a spectrum analyzer and then average RMS noise spectral density in the bandwidth $(2\tau)^{-1}$, τ being the integration constant of lock-in amplifier, is recorded around the center chopping frequency of 350 Hz. Optimal biasing conditions are found by measuring noise present in the detector at different biasing voltages and calculating corresponding values of responsivity and detectivity. Results from these measurements are plotted in fig. 29. For these measurements, the temperature of the source was kept constant at 1000°C.

From fig. 29b it can be seen that responsivity increases linearly for increasing bias voltage. Despite of this, the noise performance (D^*) levels off at higher voltages as the noise power spectral density also increases as shown in fig. 29(c) and (a). So a bias voltage of 3.5V is chosen for further measurements, as the noise performance of the detector after this value does not change significantly.

Detector's performance is measured in 3-5 μm regime with different black body temperatures (i.e. different radiation flux incident on the sample) and a constant responsivity of 49.51V/W was obtained. This responsivity is measured for the complete system including the biasing circuit and preamplifier. Also, Measured peak specific detectivity of the detector is $1.68 \times 10^5 \text{ cm}\sqrt{\text{Hz}}/\text{W}$.

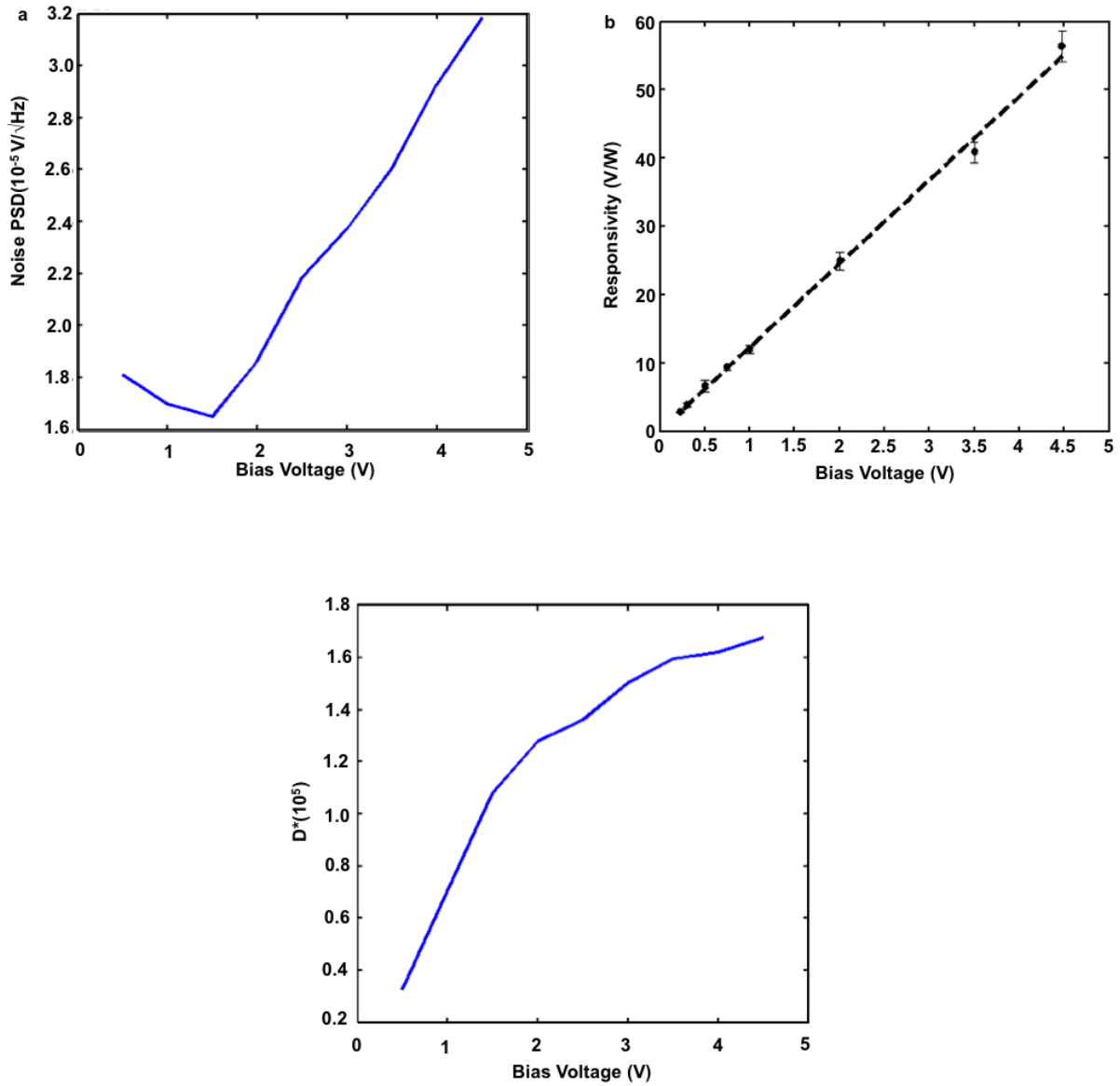


Figure 29- Parameters measured as a function of bias voltage- (a) noise power spectral density, (b) the corresponding responsivity and the (c) D^* .

4. CONCLUSION AND FUTURE SCOPE OF WORK

The two-element optical antenna system demonstrates a novel mechanism to enhance extraordinary transmission. The strong dipolar coupling between two elements enhances the transmission/absorption to $\sim 100\%$ when coupled with an optical cavity. The coupling between two antenna elements can be varied flexibly to shift the resonance location and strength. Tunability can also be exploited from the cavity phase relation, which can be simply tuned with cavity thickness. Such controlled infrared absorption when implemented in conjunction with simple large area imprinting techniques leads to development of newer classes of frequency selective low cost, uncooled infrared detectors. Our initial studies presented above have shown that a narrowband optical antenna array can alleviate some of the limitations of present IR detectors and offer significant improvements in frequency selective sensitivity and paves the path towards IR “color” imaging by pixel/sub-pixel formation with antenna -tuned to various IR bands.

4.1 Improvements in multispectral uncooled infrared radiation detector

There are several aspects of the detector under consideration that can be improved upon, for example, the time constant measurement has proved to be very difficult. Preliminary tests indicate that it is relatively large compared to traditional bolometers, which means that the source radiation should be chopped at a low frequency. But there is a limit on the low frequency imposed by the lower cutoff frequency of amplifier circuit. As we approach this frequency, the signal waveform starts to distort and it becomes very difficult to take amplitude measurements from it. It can be further improved upon by designing proper

contact lines to the detector to manage heat conduction out of the absorber pattern. Another issue with low frequency chopping of the source radiation is that light is not cutoff by the chopper wheel instantaneously and the excitation pulse to the detector is not a square wave anymore. A better choice for time constant measurement would be using AC electrical method[32] instead of traditional chopper based approach.

Detector performance can be significantly improved by reducing the noise present in the system. By reducing the detector area, i.e. by reducing the pixel size, the photon noise, which is directly proportional to the square root of the area, will decrease. This will also cause the sample resistance to go down causing the Johnson noise to decrease. Also, putting the detector chip under vacuum can reduce heat loss due to convection[33].

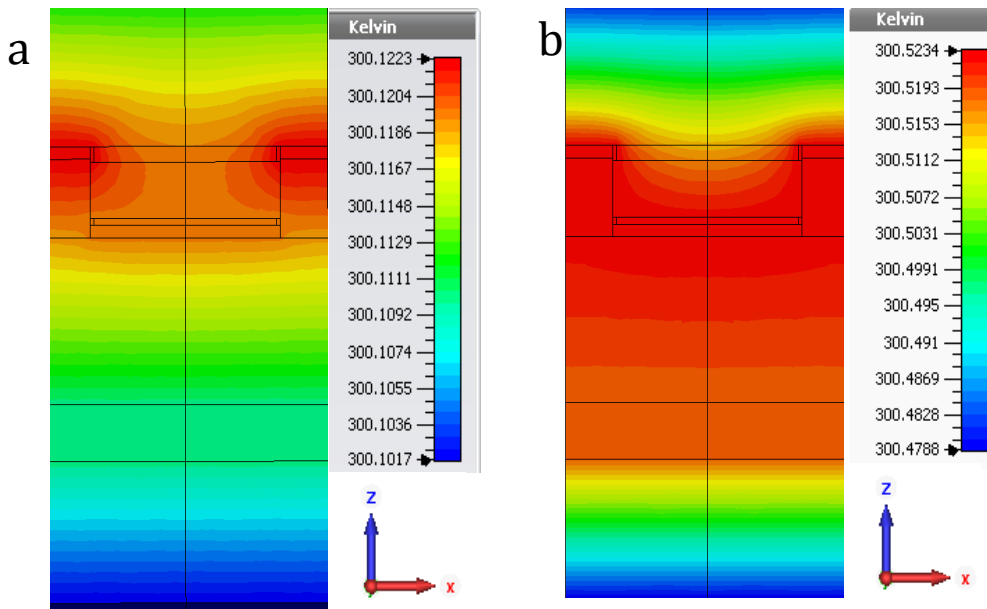


Figure 30- Predicted change in the detector temperature if the substrate is removed completely (b) compared to with substrate case(a).

Another improvement would be to thermally isolate the detector. This will greatly reduce phonon noise based on heat exchange between substrate and the detector and also reduce conductive heat loss into the substrate; therefore causing an increase in the responsivity as shown in fig. 31.

4.2 Optical Antenna as Broadband Infrared Absorber

As seen from section 1, when single layer optical antenna array is coupled with a cavity, we can obtain a narrow resonance peak with desirable properties like near perfect absorption and tunable center wavelength over the entire mid infrared regime. It is possible to construct structure with a broad bandwidth in infrared regime with similar tunability properties by simply stacking up the hole-disk antenna layers on top of each other. It was predicted that this would cause the absorption peak to split into multiple peaks forming a broadband absorber. Fig. 32 shows a schematic diagram of such 3 layer absorber and the corresponding SEM cross section. Preliminary measurements and simulation on these devices (fig. 33) show that it is indeed possible to make broadband absorber by stacking up the hole-disk antenna array. Also, from fig. 34, we can see that as we add more and more number of layers to the structure, the discrete absorption peaks take the form of a band.

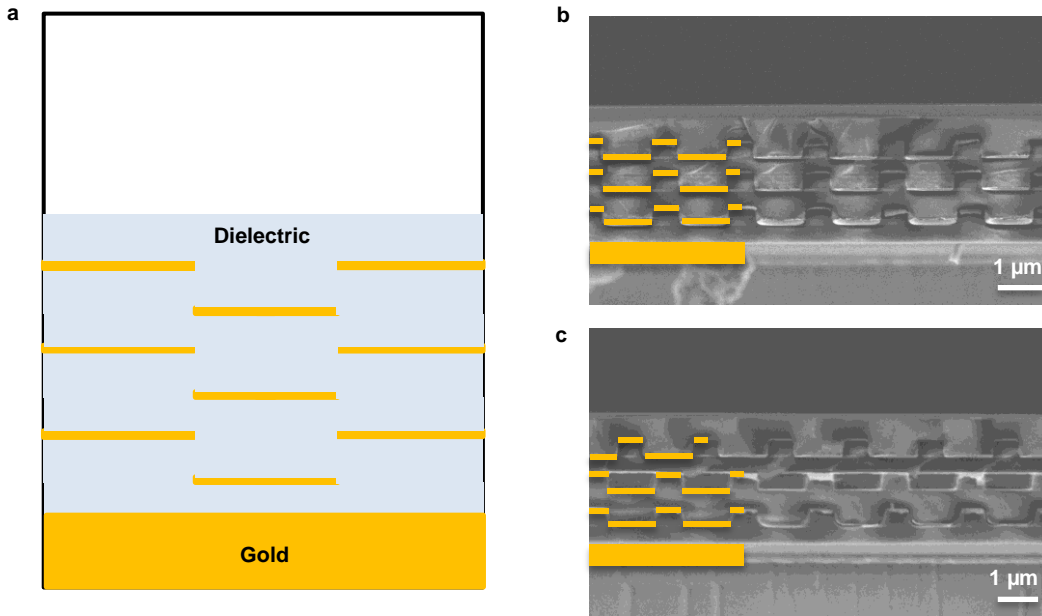


Figure 31- (a) Schematic diagram of a 3 layer hole-disk array structure, (b) and (c) SEM cross-section of fabricated structure ($P = 1740\text{nm}$, $D = 1060\text{nm}$, $RD = 300\text{nm}$ and cavity thickness $C=750\text{nm}$).

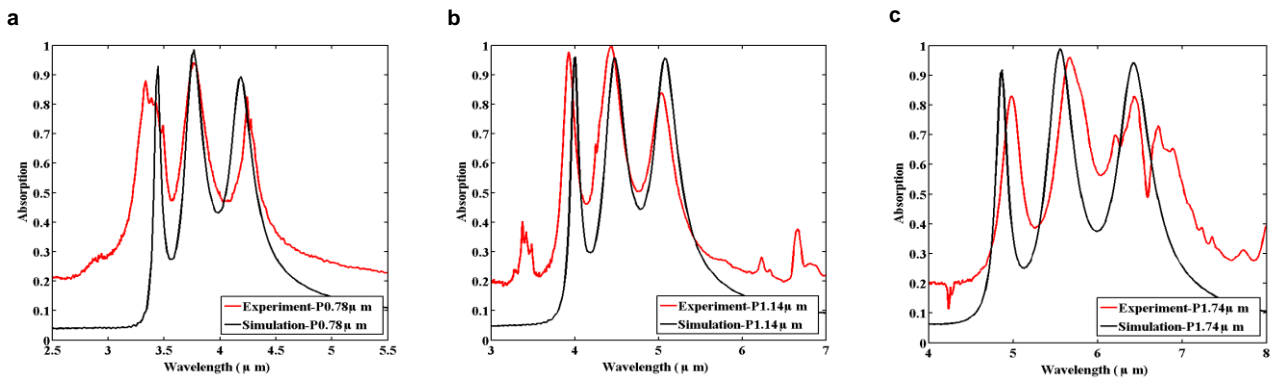


Figure 32- Simulated and measured spectra from the multilayer hole-disk structure

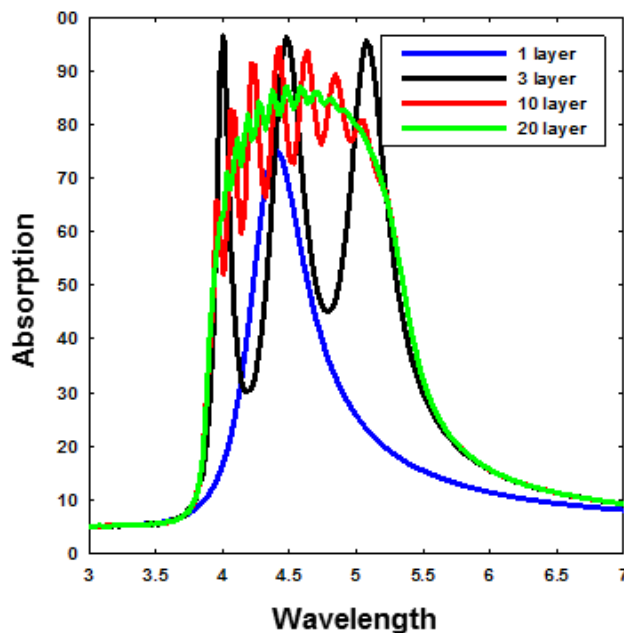


Figure 33- Simulated spectra for absorption for different number of layers in multilayer cavity coupled hole-disk antenna array

To make the structure symmetric, a thin layer dielectric is added on top of the topmost hole-disk array. It can be clearly seen that this approach of designing broadband is very effective. The bandwidth and central wavelength depends only on the transmission profile of the hole-disk array and thickness of the dielectric layer. On the basis of this preliminary data, it is desirable to study these structures more to understand and engineer tunable broadband absorbers in infrared regime.

REFERENCES

1. Rogalski, A., *Infrared detectors: an overview*. Infrared Physics & Technology, 2002. **43**(3-5): p. 187-210.
2. Park, Q.-H., *Optical antennas and plasmonics*.
3. Bharadwaj, P., B. Deutsch, and L. Novotny, *Optical Antennas*. VIRGINIA QUARTERLY REVIEW, 2008. **84**(4): p. 438-483.
4. Codreanu, I., F.J. Gonzalez, and G.D. Boreman, *Detection mechanisms in microstrip dipole antenna-coupled infrared detectors*. Infrared Physics & Technology, 2003. **44**(3): p. 155-163.
5. Middlebrook, C., et al., *Infrared antenna-coupled phased-array*. 2007, Orlando, Fla: University of Central Florida.
6. Codreanu, I.a.B., G. D., *Infrared microstrip dipole antennas—FDTD predictions versus experiment*. Microwave and Optical Technology Letters, 2001. **29**(6).
7. Corkish, R., M.A. Green, and T. Puzzer, *Solar energy collection by antennas*. Solar Energy, 2002. **73**(6): p. 395-401.
8. Briones, E., J. Alda, and F.J. Gonzalez, *Conversion efficiency of broad-band rectennas for solar energy harvesting applications*. Opt Express, 2013. **21 Suppl 3**: p. A412-8.
9. Niesler, F.B.P., et al., *Metamaterial metal-based bolometers*. Applied Physics Letters, 2012. **100**(20): p. 203508.
10. Ebbesen, T.W., et al., *Extraordinary optical transmission through sub-wavelength hole arrays*. Nature, 1998. **391**(6668): p. 667.

11. Chang, S.H., S.K. Gray, and G.C. Schatz, *Surface plasmon generation and light transmission by isolated nanoholes and arrays of nanoholes in thin metal films*. OPTICS EXPRESS, 2005. **13**(8): p. 3150-3165.
12. Thio, T., et al., *Surface-plasmon-enhanced transmission through hole arrays in Cr films*. JOURNAL OF THE OPTICAL SOCIETY OF AMERICA B-OPTICAL PHYSICS, 1999. **16**(10): p. 1743-1748.
13. Rogobete, L., et al., *Design of plasmonic nanoantennae for enhancing spontaneous emission*. Opt Lett, 2007. **32**(12): p. 1623-5.
14. Javier Alda, J.e.M.R.-G.i., Jos'e M L'opez-Alonso, G. Boreman, *Optical antennas for nano-photonics applications*. Nanotechnology, 2005.
15. Alu, A. and N. Engheta, *Theory, Modeling and Features of Optical Nanoantennas*. IEEE Transactions on Antennas & Propagation, 2013. **61**(4): p. 1508-1517.
16. Jackson, J.D., *Classical electrodynamics*. 1962: New York, Wiley 1962.
17. Zhao, L.L., K.L. Kelly, and G.C. Schatz, *The extinction spectra of silver nanoparticle arrays: Influence of array structure on plasmon resonance wavelength and width*. JOURNAL OF PHYSICAL CHEMISTRY B, 2003. **107**(30): p. 7343-7350.
18. Myroshnychenko, V., et al., *Modelling the optical response of gold nanoparticles*. CHEMICAL SOCIETY REVIEWS, 2008. **37**(9): p. 1792-1805.
19. Thongrattanasiri, S., F.H.L. Koppens, and F.J.G. de Abajo, *Complete Optical Absorption in Periodically Patterned Graphene*. PHYSICAL REVIEW LETTERS, 2012. **108**(4).

20. Bohren, C.F. and D.R. Huffman, *Absorption and scattering of light by small particles / Craig F. Bohren, Donald R. Huffman*. Wiley science paperback series. 1983: New York : Wiley, c1983.
21. Smith, D.R., et al., *Determination of Effective Permittivity and Permeability of Metamaterials from Reflection and Transmission Coefficients*. 2001.
22. Chen, X.D., et al., *Robust method to retrieve the constitutive effective parameters of metamaterials*. PHYSICAL REVIEW E, 2004. **70**(1).
23. Chanda, D., et al., *Coupling of plasmonic and optical cavity modes in quasi-three-dimensional plasmonic crystals*. Nature Communications, 2011. **2**: p. Article.
24. C, C.T., *Effective Medium Theory*. 1999, Oxford: Clarendon Press.
25. Novotny, L., *Effective wavelength scaling for optical antennas*. Phys Rev Lett, 2007. **98**(26): p. 266802.
26. Wang, M. and N. Pan, *Predictions of effective physical properties of complex multiphase materials*. Materials Science & Engineering R-Reports, 2008. **63**(1): p. 1-30.
27. Wenshan. Cai, S.V., *Optical Metamaterials: Fundamentals and Applications*. 2009, Springer.
28. Richards, P.L., *Bolometers for infrared and millimeter waves*. Journal of Applied Physics, 1994. **76**(1): p. 1.
29. E. L. Dereniak, G.D.B., *Infrared Detectors and Systems*. John Wiley & Sons, Inc.
30. Purkl, F., et al., *Serpentine geometry for enhanced performance of nanometer-thin platinum bolometers*. 2013 Transducers & Eurosensors XXVII: The 17th

- International Conference on Solid-State Sensors, Actuators & Microsystems (TRANSDUCERS & EUROSENSORS XXVII), 2013: p. 1507.
31. Kruse, P.W., *Uncooled thermal imaging : arrays, systems, and applications / Paul W. Kruse*. Tutorial texts in optical engineering: v. TT 51. 2001: Bellingham, Wash., USA : SPIE Press, c2001.
 32. Ou-Yang, M. and C.-S. Sheen, *Parameter Extraction of Resistive Thermal Microsensors by AC Electrical Method*. IEEE Transactions on Instrumentation & Measurement, 1998. **47**(2): p. 403.
 33. Liddiard, K.C., *Thin-film resistance bolometer IR detectors*. Infrared Physics, 1984. **24**: p. 57-64.
 34. Bendickson, J.M., J.P. Dowling, and M. Scalora, *Analytic expressions for the electromagnetic mode density in finite, one-dimensional, photonic band-gap structures*. PHYSICAL REVIEW E, 1996. **53**(4): p. 4107-4121.
 35. Gadsdon, M.R., J. Parsons, and J.R. Sambles, *Electromagnetic resonances of a multilayer metal-dielectric stack*. Journal of the Optical Society of America B, 2009. **26**(4): p. 734-742.
 36. Sprung, D.W.L. and W. Hua, *Scattering by a finite periodic potential*. American Journal of Physics, 1993(12): p. 1118.
 37. Scalora, M., et al., *Transparent, metallo-dielectric, one-dimensional, photonic band-gap structures*. Journal of Applied Physics, 1998. **83**(5): p. 2377.